Available online at www.sciencedirect.com
ScienceDirect
Trans. Nonferrous Met. Soc. China 31(2021) 2626−2650
Transactions of Nonferrous Metals Society of China
www.tnmsc.cn

Simulation and experimental study of dynamic recrystallization process during friction stir vibration welding of magnesium alloys

Mahmoud ABBASI[1], Behrouz BAGHERI[2], Farzaneh SHARIFI[3]

1. Faculty of Engineering, University of Kashan, Kashan, Iran;
2. Department of Mining and Metallurgy, Amirkabir University of Technology, Tehran, Iran;
3. School of Mechanical and Materials Engineering, Washington State University, Pullman, USA

Received 24 July 2020; accepted 5 July 2021

Abstract: A two-dimensional cellular automaton (CA) model was utilized to analyze the effect of mechanical vibration on microstructure evolution of AZ91 alloy during friction stir welding (FSW). The simulated results, namely grain topology, grain size distribution, average grain size, and also the dynamic recrystallization (DRX) fraction were compared with measured data. The adequate comparability between FEM and experimental data shows that the CA method can be applied to the analysis of the microstructure progression during the friction stir welding of AZ91 alloy. It is concluded that the dislocation density during the friction stir vibration welding (FSVW) is higher than that in the FSW process and the process of nucleation and grain growth is faster for samples during FSVW compared to FSW. The grain size modification and DRX phenomenon with various vibration frequencies were also simulated in detail during FSVW. It is found that vibration makes nucleation start earlier and decreases the proportion of the incubation period and the percentage of recrystallization as vibration frequency improves.

Key words: friction stir welding; vibration; simulation; grain size; dynamic recrystallization; cellular automaton model

1 Introduction

Magnesium alloys have the merits of light-weight and special mechanical characteristics such as high specific strength, and therefore they show a great application in structure manufacturing in the transportation, aerospace, automotive, and other important industries [1,2]. Friction stir welding (FSW) can be considered an efficient means to qualify the structure of metal materials [3]. The FSW process has been now implemented in numerous industries, including automotive, aerospace, shipbuilding, to joint different metals namely Cu, Al, and Mg classified as being essentially difficult to weld with typical welding methods [4]. In the past years, various researches have been conducted on mechanical performance and microstructures of the welded sample from several perspectives such as static, dynamic, residual stress, cracks propagation, wear, fatigue, and corrosion resistance. In addition, the impact of the most significant welding parameters on the effectiveness of the generated weld has been investigated with the aim to improve the mechanical characteristics of the joint samples [5−10].

The mechanical characteristics of a joint area such as tensile strength, hardness and toughness, are fundamentally influenced by the grain size and a microstructure including fine grains will improve these properties. Experimental measurement of microstructure evolution in the joint area is demanding and time-consuming, while the numerical analyses are very effective and reasonable for various plastic deformation processes. Recently, finite element analysis (FEA)

Corresponding author: Behrouz BAGHERI, E-mail: b.bagheri@aut.ac.ir
DOI: 10.1016/S1003-6326(21)65681-9

has been applied to simulating friction stir welding to define the relationship among various welding parameters of weld strength, temperature, and material flow. KEIVANI et al [11] employed the finite element method (FEM) to investigate the influence of preheating and pin angle on temperature history during FSW. The pin geometry and thermal analysis during the friction stir welding process were examined by ABBASI et al [12]. It was indicated that the spherical pin compared to other pin shapes provides the highest temperature profile at weldment. MARZBAND et al [13] utilized the simulation method to examine the influence of friction stir welding parameters like welding tool pin geometry on mechanical characteristics and material flow at the workpiece. The grain size in the stir zone (SZ) is of great importance to examine the mechanical and thermal characteristics of the weld during the friction stir welding [14]. Because of the difficulty and time-consuming measurement of grain size in the joint area experimentally, the use of the finite element method (FEM) is reasonable. Given the changeable nature of the dynamic recrystallization (DRX) phenomenon, DRX includes the influences of precipitations, grain boundary motion, dislocation movement, and impurities. Nevertheless, recrystallized grains are bound to terminate to grow as the deformation of material increases, which influences decreasing the discrepancy of dislocation density. The microstructure parameter, particularly the grain size, changes with the welding condition. Consequently, knowing the DRX is fundamental when trying to measure the mechanical characteristics of weld material. In order to determine the quality of friction stir welding, grain growth in weld samples is a significant factor. Therefore, investigations have been concentrated on the grain evolution in the friction stir welding process. Numerous experimental studies have explained the relations between service performances of joints and final grain characteristics. There are different useful methods to analyze the microstructure evolution during FSW, including the phase-field (PF) method, the cellular automaton (CA) method, the Monte Carlo (MC) method, etc [15−17]. All these methods, although, successfully model microstructural evolution, the cellular automaton model has attracted more attention of researchers because of its straightforward employment time and length scale calibrations as well. The cellular automaton technique has been applied to simulating static recrystallization and also dynamic recrystallization. This method considers the uniform distribution of stored energy in the material and determines accordingly the nucleation standards for recrystallization analysis. Numerous researchers have pointed out that the cellular automaton model proposes a computationally productive framework regarding the finite element analysis of microstructural evolution during the plastic deformation such as the welding process. The cellular automaton method was used by AFSHARI and SERAJZADEH [18] to investigate the static recrystallization of low carbon steel during cold pressing. The dynamic recrystallization process, during FSW, was simulated by ASADI et al [19]. They modeled the dislocation accumulation map, nucleation process, and grain growth steps of dynamic recrystallization during the FSW process.

The combination of temperature variation and the effective strain of joints can play a permanent role in determining the grain size and consequently, the mechanical performance of the weld sample after the welding process. Up to now, different experimental researches have been performed to improve FSW and develop the efficiency of the process. Researchers have studied to implement ultrasonic vibration to assist the FSW process to achieve significant results in different plastic forming processes [20−22]. Ultrasonic energy can influence the heat generation and material flow during the FSW process, which plays a prominent role in the evolution of the microstructure and improvement in the mechanical performance of joints [23−25]. LIU et al [26] applied the ultrasonic-assisted friction stir welding (UVeFSW) method. It was shown that the mechanical characteristics and the size of the weld zone improved while grain size in the weld area was reduced. The ultrasonic vibration was used by SHI et al [27] to increase the mechanical performance of the Al joint during friction stir welding with various rotational and traverse speeds. They concluded that the traverse torque and tool force magnitudes decreased as ultrasonic vibration was used during the welding process. The reduction of friction because of using ultrasonic vibration during the friction stir welding was analyzed by YANG

et al [28]. They found that the heat input, during friction stir welding process, is more noticeable by considering the ultrasonic induced friction reduction (UiFR). ZHAO et al [29] modified the traditional Norton friction method with the acoustic stress and analyzed the impact of ultrasonic-vibration on the interface area between the welding tool and weldment. They indicated that ultrasonic wave can decrease the friction stress in the interface area and results in the material flow, heat generation, and temperature distribution during the ultrasonic-assisted friction stir welding process.

Less attempt has been carried out to simulate the impact of mechanical vibration on the dynamic recrystallization evolution. In the present study, an improved version of FSW is studied. In this model, by friction stir vibration welding (FSVW), the weldment is vibrated normal to the weld tool axis as the tool rotates during FSW. To model the microstructural evolutions of AZ91 alloy during FSVW, the analysis was done in two separate steps: first, a continuum-based thermo-mechanically coupled rigid viscoplastic FEM technique for FSVW was determined, and then the advanced model for microstructure analysis was coupled to FSVW simulation model inDeform-3D software. The nucleation and grain growth steps in the stir zone (SZ) were shown and compared with experimental data. The effect of vibration frequency on microstructure evolution was considered in both experiment and simulation methods.

2 Experimental

2.1 Materials

In this examination, as-received AZ91 sheet metal as a workpiece having a thickness of 3 mm, a length of 200 mm and a width of 100 mm. Table 1 displays the chemical composition of the examined sheet.

Friction stir vibration welding was considered by introducing vibration normal to the weld direction through a fixture inserted beneath the weldment in FSW. To control the rotation movement of the motor shaft to the liner, a camshaft was implemented in the vibrating machine. Figure 1 presents the view design of the FSVW method. In this work, the amplitude of vibration is 0.6 mm, and also the vibration frequency was controlled by the driver for various welding conditions. In this study, vibration frequency, rotational speed, and traverse velocity were 38 Hz, 950 r/min, and 63 mm/min, respectively.

Table 2 presents the properties of the tool applied in this study. The outsides of samples had been sand-blasted to remove surface oxides and then they were etched by a liquid of acetic acid (5 mL), water (10 mm), nitric acid (7 mL), picric acid (6 g), ethanol (100 mL), and HCL (5 mL) for

Table 1 Chemical composition of analyzed AZ91 alloy (wt.%)

Mg	Al	Zn	Mn	Si	Fe	Cu	Ni
Bal.	9.1	0.68	0.21	0.085	0.0029	0.0097	0.001

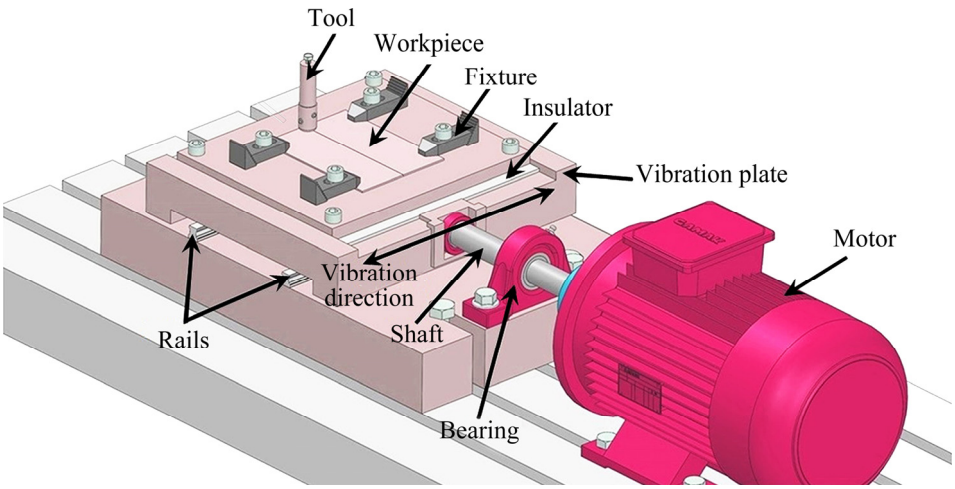

Fig. 1 Machine used for friction stir vibration welding, and applied welding tool and fixture set

Table 2 Tool welding characteristics for FSW

Parameter	Value or description
Axial pressure, P_T/MPa	25.5
Tool material	PCBN
Density of welding tool/(kg·m^{-3})	3120
Thermal conductivity of welding tool/(W·K^{-1})	130
Specific heat capacity of welding tool/(J·kg^{-1}·K^{-1})	1966
Tilt angle/(°)	3
Diameter of welding tool shoulder/mm	12
Diameter of welding tool pin/mm	4
Welding tool pin height/mm	2.8

3−5 s. The method of conventional linear intercept has been carried out to measure the grain size. To analyze the temperature distribution during the welding, an infrared thermometer with ±5 °C accuracy was used. Optical microscopy (OM) was applied to analyzing the microstructures. To study the flow stress of the workpiece, a hot compression test with two strain rates (0.1 and 1 s^{-1})) was carried out. The tests were done on a Gleeble−1500 thermomechanical simulator by holding a furnace with ±5 °C accuracy, in a temperature range of 325−400 °C under a fixed ram speed of 0.6−600 mm/min. Hot compression test, after immersing for 3 min at test temperature, was done up to a strain of 0.7. The contact surfaces, to decrease the friction, were wrapped through Teflon layers. The specimens were water quenched, after testing, within 5 s to preserve the hot deformation microstructure. The samples were heated to the test temperature with a heating rate of 15 °C/min before loading.

2.2 FEM model

In this investigation, because of severe plastic deformation processes and a high level of mesh distortion during FSW, Deform-3D™ software was applied. To simplify the analysis, the welding tool was considered as a rigid part, and to increase the precision of calculation, fine elements in mean size of 0.5 mm were used around the tool along the weld line. Anon-uniform mesh of about 22000 and 73000 for tool and workpiece with an automatic remeshing ability were used, respectively. Figure 2 shows the schematic of the meshed model and also a boundary condition used in this simulation. To improve the compatibility between experiment and simulation results, a shear friction coefficient of 0.3 was applied. In this study, a positive pressure for the interaction of the two mutual contact materials was considered. The corresponding speed of the stirring head and joining sheet is not determined. Since the contact area between the top surface of the weldment body and the joining fixture is small, the heat conduction was negligible. Convective heat transfer with air was determined for all surfaces of the workpiece (15 W·m^{-2}·K^{-1}), while the convection coefficient of the bottom surface due to putting on a backup was set to be 30 W·m^{-2}·K^{-1} to calculate the heat loss of thermal conductivity. The displacement for the bottom surface of the weldment in three directions (x, y and z) was zero during the first step of the conventional thermomechanical process. For other main steps of welding, based on Fig. 1 and the application of vibration in the x-direction (perpendicular to the welding direction), the displacement of the workpiece bottom for only two directions including y and z was restricted. The finite element model (FEM) was produced to be a DB file and then selected for the solving processor. In this analysis, the time step size was 0.2 s, and also the Newton–Raphson iteration technique was determined to analyze the finite element method (FEM) computation time.

The mean velocity on friction area would be determined based on Eq. (1) [30]:

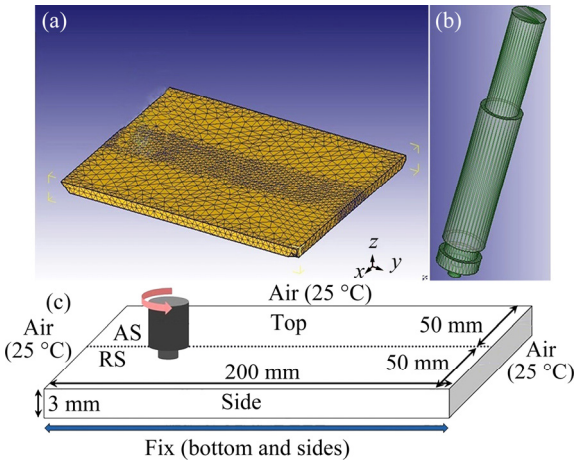

Fig. 2 View of simulation model: (a) Workpiece; (b) Tool; (c) Initial boundary conditions (AS−Advanced side; RS−Retreat side)

$$v_f=(R_{out}+R_{in})\omega/2 \quad (1)$$

where R_{out} indicates the radius of the tool shoulder ($R_{shoulder}$), ω indicates the rotation speed of joining, and R_{in} shows the radius of the tool pin (R_{pin}).

In friction stir welding, the strain rate and velocity are defined by the following formula:

$$\{\dot{\varepsilon}\}=[L]\{\dot{u}\} \quad (2)$$

$$[L]=\begin{bmatrix} \frac{\partial}{\partial x} & 0 & 0 & \frac{\partial}{\partial y} & 0 & \frac{\partial}{\partial z} \\ 0 & \frac{\partial}{\partial y} & 0 & \frac{\partial}{\partial x} & \frac{\partial}{\partial z} & 0 \\ 0 & 0 & \frac{\partial}{\partial z} & 0 & \frac{\partial}{\partial y} & \frac{\partial}{\partial x} \end{bmatrix} \quad (3)$$

where $\{\dot{\varepsilon}\}$ shows the strain rate matrix, $[L]$ is the geometric stiffness matrix, and $\{\dot{u}\}$ indicates the displacement rate matrix.

2.3 Constitutive equation

To explain the strain rate, the flow stress, and also the temperature values during severe hot deformation, the modified Arrhenius constitutive equation with respect to flow stress and Zener–Hollomon (Z) parameter is generally applied. A hyperbolic sine in the Z−A model can be defined as [31]

$$\begin{cases} \sigma_{(\varepsilon)}=\dfrac{1}{\alpha(\varepsilon)}\left\{\left[\dfrac{Z}{A_{(\varepsilon)}}\right]^{1/n_{(\varepsilon)}}+\left[\left(\dfrac{Z}{A_{(\varepsilon)}}\right)^{2/n_{(\varepsilon)}}+1\right]^{1/2}\right\} \\ Z=\dot{\varepsilon}\exp[Q_{(\varepsilon)}/(RT)] \end{cases} \quad (4)$$

where ε indicates the strain rate, σ indicates the flow stress, Q indicates the activation energy of the Mg alloy during hot deformation, R is the gas constant, T is the absolute temperature, and A, n and α indicate the material constants. Table 3 presents the thermal properties of the AZ91 alloy applied in this modeling. Figure 3 shows the true stress−strain curves achieved from the isothermal compression test (temperature of 200−400 °C and strain rates of 0.1 and 1 s^{-1}). It is seen that the flow stress profile firstly rises to the maximum value and after that falls slowly to steady-state stress as the strain develops. This flow model is a common DRX softening characteristically related to the work hardening. And the critical stress, maximum stress, and steady-state stress improve with reducing the temperature and improving the strain rate.

Table 3 Thermal properties and Arrhenius coefficients of AZ91 alloy

Property or coefficient	Value
Heat capacity/(N·mm^{-2}·°C^{-1})	2.096
Emissivity	0.12
A	2.8405×10^{12}
α	0.021
n	5.578
Q/(kJ·mol^{-1})	1.47
R/(J·K^{-1}·mol^{-1})	8.314472

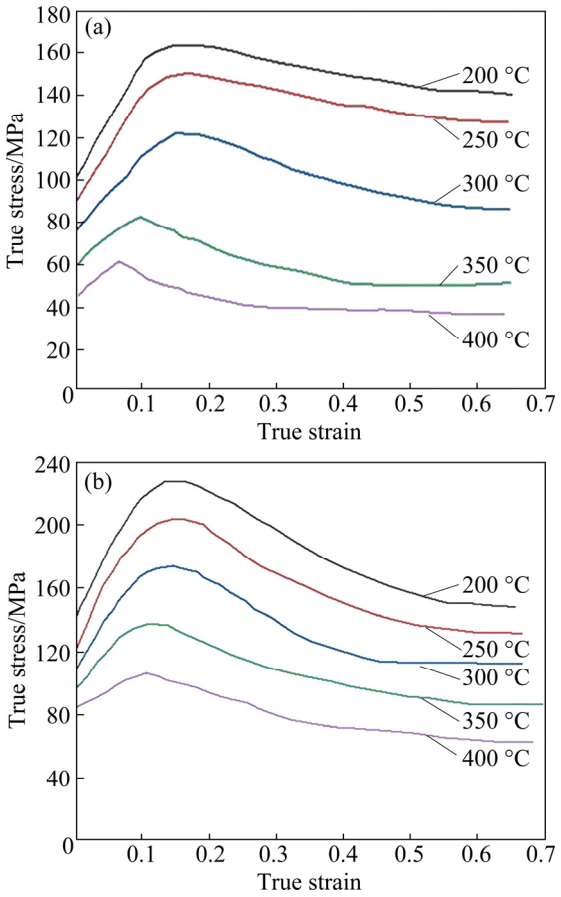

Fig. 3 True stress−strain curves from compression analysis for various strain rates and temperatures: (a) 0.1 s^{-1}; (b) 1 s^{-1}

2.4 Cellular automaton (CA) model

The cellular automaton (CA) method is well-known as a crucial technology for analyzing the microstructure in recent years. The fundamental idea of the cellular automaton model is to explain the assignment of complicated operations with the discrete-time and space behavior by installing deterministic or possibility transformation rules toward cells in the vicinity [32]. A cellular

automaton model involves the five components, namely cells, cellular state, cellular space, neighbor type, and transformation rules. Figure 4 shows an interaction between macroscopic and mesoscopic evolution for the CA method. According to Fig. 4, there is a multiscale modeling relationship between mesoscopic microstructures and macroscopic thermomechanical properties through dislocation density. And also, there is a diversity of flow stress along with the mean dislocation density of the materials and continuous dislocation density at a single cell of the cellular automaton. During the cellular automaton model, a complicated system is classified into a finite number of cells. Besides, the time is discretized into numerous time steps including a specific interval. Then, the feasible states of each cell are distributed into a finite number of certain states. Based on specific evolution rules, the state transition of the cell regarding each time step is recognized. Because of the synchronizing of the transformation with each cell over time, the state of a cell is influenced through the states of the vicinity cells, and simultaneously, it also influences the states of vicinity cells [33].

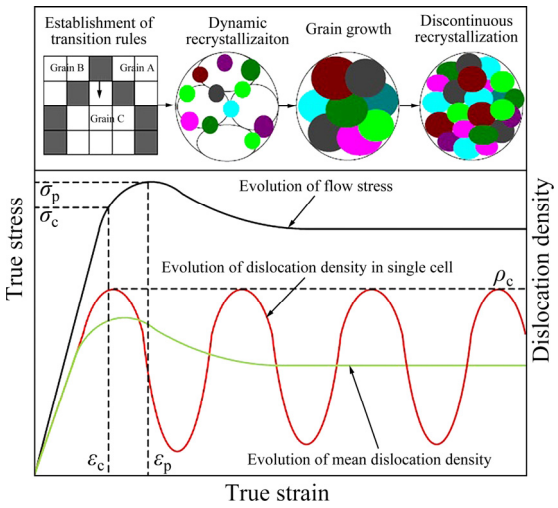

Fig. 4 Interaction between macroscopic and mesoscopic evolution for CA method [34]

2.4.1 Modeling of dislocation density

After the welding process, the dislocation density distribution is also assigned by two various transition rules. The first rule is by Eq. (5) which indicates the grain size regarding dislocation density. This special equation is achieved from the relationships between dislocation density and flow stress, and grain size and flow stress from the examination of AKBARI et al [35]. Based on the second rule, the dislocation density is estimated using an experimental model achieved from the empirical measurements by PROSGOLITIS et al [17] with respect to dislocation density and grain size diversity across the joint area. This equation is a fourth-order polynomial fit between dislocation density (ρ) and grain size (D) across the joint area [17]. Based on AKBARI et al [35], the relationship between dislocation density and grain size after the FSW can be defined as

$$\rho=\left(\frac{k'}{\alpha' Eb}\right)^2 D_{\mathrm{RDX}}^{-1} \tag{5}$$

where ρ indicates the dislocation density, k' and α' are equation constants, b indicates the magnitude of burgers vectors, E is the elastic modulus, and D_{RDX} relates to the grain size after the FSW process. Based on Eq. (5), there is an adverse relationship between dislocation and grain size for a sample produced by FSW.

Dislocations during the severe plastic deformation are produced due to work hardening and annihilated through the dynamic recovery (softening effect), and therefore, the mean dislocation density is considered as

$$\mathrm{d}\rho/\mathrm{d}\varepsilon=(\mathrm{d}\rho/\mathrm{d}\varepsilon)_{\mathrm{hard}}+(\mathrm{d}\rho/\mathrm{d}\varepsilon)_{\mathrm{soft}} \tag{6}$$

The density of dislocation motion barriers is considered as [35]

$$1/l=1/\zeta d+1/\beta\rho^{-1/2} \tag{7}$$

where d is related to the distance of the obstacles, and ζ and β indicate the numeric factors regarding l (dislocation mean free path).

During the dislocation progression equation, the dislocation accumulation is M'/bl (M' is related to the Taylor factor) [36]. The empirical equation is given as

$$\mathrm{d}\rho/\mathrm{d}\varepsilon=k_1\rho^{-1/2}-k_2\rho \tag{8}$$

where k_1 and k_2 indicate work hardening and the softening parameter that resubmits the recovery of dislocation, respectively.

Also, k_1 and k_2 can be defined as

$$\begin{cases} k_1=2\theta_0/(\alpha_{\mathrm{f}}\mu b) \\ k_2=2\theta_0/\sigma_{\mathrm{s}} \end{cases} \tag{9}$$

where α_{f} indicates a dislocation interaction term that considers the amplitude of $0.5\theta_0$ (θ_0 indicates the

hardening rate that expresses the slope of the empirical flow stress diagram). μ is the shear modulus. This value is constant (μ/200) at a particular temperature. The particular form of σ_s is also obtained from the empirical achievements. The geometrical dislocation (GD) density is associated with the grain size, and regarding fine-grained structure, the geometrical dislocations principally affect the density of dislocations in thermomechanical processing which modify the plastic deformation among grains. The fundamental dislocation free path may be classified with the spacing between these geometric barriers as [37]

$$d\rho/d\varepsilon=k_1\rho^{1/2}+1/bd'-k_2\rho \tag{10}$$

where d' indicates the mean grain size, involving basic and DRX grains.

The softening phenomenon is attributed to the DRX during the deformation process:

$$f_{DRX}=\frac{\Delta\sigma}{\Delta\sigma_m} \tag{11}$$

where f_{DRX} is the volume fraction of DRX grains, $\Delta\sigma$ is the net softening value, and $\Delta\sigma_m$ indicates the maximum softening value.

The flow stress is related to the strain because of the dislocation/dislocation interaction [38]:

$$\sigma=\alpha_f\mu b\rho^{1/2} \tag{12}$$

Regarding a deforming structure, the discrepancy of its dislocation density may be measured by Eq. (10) from the start of deformation. New nuclei appear on the grain boundary as its amplitude hits the critical dislocation density toward the nucleation of DRX. With respect to the DRX grains, the dislocation density has been fundamentally considered to be zero and then improves as the deformation process proceeds. The dislocation density change of DRX grains is measured by employing Eq. (10). During the growth of DRX grain, the driving force reduces continuously as its dislocation density improves by deformation. The grain growth stops as the driving force equals zero. When the dislocation density for a DRX grain equals the critical amplitude for the DRX nucleation process, its boundaries can also be performed as nucleation sites.

During the deforming process, in order to estimate the flow stress, a mean dislocation density assuming the dislocation densities of the structure and all the DRX grains is applied:

$$\rho=\rho_m(1-f_{DRX})+f_{DRX}\sum_{i=1}^{N}\rho_i(V_i/V) \tag{13}$$

where ρ_i is the dislocation density of the ith DRX grain and ρ_m is the dislocation density of matrix at a specific time. V_i and V indicate the volume of the ith DRX grain and the comprehensive volume of whole DRX grains at a specific time, respectively, and N is the number of entire DRX grains.

2.4.2 Nucleation and grain growth model

The kinetics of DRX modification is given as [38]

$$f_{DRX}=1-\exp[k(\frac{\varepsilon-\varepsilon_c}{\varepsilon^*})^n] \tag{14}$$

where ε^* indicates the strain for the highest softening rate, ε_c indicates the critical strain value, and k and n indicate the material constants.

In the finite element analysis, a critical strain according to the size of the subgrain, initial grain and grain shape, can be determined as

$$\varepsilon_{cr}=\ln\left(\frac{K_1D_0f_s}{\delta_{ss}}\right) \tag{15}$$

where K_1 is the material constant, D_0 indicates the initial grain size, f_s indicates the shape factor (f_s is the ratio of max size to min size) and δ_{ss} indicates the sub-grain size. Therefore, the DRX evolution kinetics of the AZ alloys would be determined as [39]

$$\begin{cases} k=\exp[-1.37309236+0.00745888\ln(Z/A)+\\ \quad 0.02248822\ln(Z/A)^2] \\ n=\exp[0.7448719+0.09481055\ln(Z/A)-\\ \quad 0.0054608\ln(Z/A)^2] \\ \varepsilon_c=0.0334(Z/A)^{0.0804} \\ \varepsilon^*=0.1633(Z/A)^{0.1209} \\ \varepsilon_p=0.0751(Z/A)^{0.1371} \\ A=1.59\times10^{14} \\ Z=\dot{\varepsilon}\exp(\frac{181980}{8.31T}) \end{cases} \tag{16}$$

where ε_p denotes the strain corresponding to the peak stress (σ_p).

The nucleation rate of per unit grain boundary area during the DRX process is given as [40]

$$\dot{n}(\dot{\varepsilon},T)=C\dot{\varepsilon}\exp\left(\frac{-Q_{act}}{RT}\right) \tag{17}$$

where Q_{act} indicates the activation energy, and C

indicates the material constant.

The critical dislocation density can be defined as [41]

$$\rho_c = \frac{20\gamma_i^{\dot{\varepsilon}}}{3blM\tau^2} \tag{18}$$

where γ_i indicates the energy of grain boundary, τ indicates the dislocation line energy equal to $0.5\mu b^2$, and M indicates the grain boundary motion.

The growth velocity V_i for the ith DRX grain can be defined as

$$v_i = MF_i/(4\pi r_i^2) \tag{19}$$

where F_i indicates the driving force regarding the ith DRX grain with radius r_i.

It is worth noting that the grain boundary mobility (M) of low angle boundaries (LABs) needs a climbing of dislocations in the boundary [41]:

$$\begin{cases} M = D_s b/(k_B T) \\ \delta D_s = \delta D_{0s} \exp[-Q_s/(RT)] \end{cases} \tag{20}$$

where δ indicates the property regarding grain boundary thickness, Q_s indicates the self-diffusion activation energy, D_s indicates the self-diffusion coefficient, D_{0s} indicates the pre-exponential factor, and k_B indicates the Boltzmann's constant.

The energy change as the radius of a grain r_i grows equal to dr_i can be defined as [42]

$$\mathrm{d}W_i = \mathrm{d}W_i^{\mathrm{sur}} + \mathrm{d}W_i^{\mathrm{vol}} \tag{21}$$

where $\mathrm{d}W_i^{\mathrm{sur}}$ indicates the grain boundary energy variation, while $\mathrm{d}W_i^{\mathrm{vol}}$ indicates the dislocation energy modification due to the grain growth. Therefore,

$$\begin{cases} \mathrm{d}W_i^{\mathrm{sur}} = -\mathrm{d}(4\pi r_i^2 \gamma_i) = -8\pi r_i \gamma_i \mathrm{d}r_i \\ \mathrm{d}W_i^{\mathrm{vol}} = 4\pi r_i^2 \tau(\rho_m - \rho_i)\mathrm{d}r_i \end{cases} \tag{22}$$

To determine the size of recrystallized grains, the equivalent average radius of a grain (r_{re}) is applied:

$$r_{re} = \sqrt{\frac{N_i A_{cell}}{\pi}} \tag{23}$$

where A_{cell} is the area of one cell and N_i is the number of cells with respect to the recrystallized grains.

The driving force can be defined as

$$F_i = 4\pi r_i^2 \tau(\rho_m - \rho_i) - 8\pi r_i \gamma_i \tag{24}$$

According to the Read−Shockly equation, the grain boundary energy is defined as [43]

$$\gamma_i = \begin{cases} \gamma_m, \ \theta_i \geq 15° \\ \gamma_m \dfrac{\theta_i}{\theta_m}\left(1 - \ln\left(\dfrac{\theta_i}{\theta_m}\right)\right), \ \theta_i < 15° \end{cases} \tag{25}$$

where θ_i indicates the misorientation for the ith DRX grain and its neighboring grain.

According to Eq. (25), the grain boundary energy with respect to high angle boundary (HABs) is defined as

$$\gamma_m = \frac{b\mu\theta_m}{4\pi(1-\upsilon)} \tag{26}$$

where γ_m indicates the boundary energy, θ_m indicates the misorientation of grain boundary for high angle boundary, and υ indicates Poisson's ratio. The values of the required input parameters of AZ91 alloy are presented in Table 4.

To confirm the obtained grain size and also recrystallization kinetics, the CA steps have to convert into real-time. The time step of the finite element analysis has been analyzed by stored energy and length scale of the cell (L_{CA}):

$$\Delta t = \frac{k_B T L_{CA}}{Z' D_0 b^2 P \exp\left(\dfrac{-Q_b}{RT}\right)} \tag{27}$$

where P indicates the driving pressure for the recrystallization, Z' indicates the pinning effect, and Q_b is the activation energy.

Table 4 Input parameters for simulation of CA model [39]

Parameter	Value
b/m	6.12×10^{-10}
μ/Pa	1.70×10^{10}
υ	0.35
D_0/(m^2·s^{-1})	200.78
Q_b/(J·mol^{-1})	134.21
ρ_0/μm^{-2}	0.01
Strain rate sensitivity, m	0.2
k_B	6030

2.4.3 Accomplishment of recrystallization in CA method

In the center of the joining zone, the location of the CA cell was considered. Each lattice includes four different variables: one variable for orientation

that indicates the orientation of grain and measures the energy of grain boundary, one variable for status showing which grain is recrystallized, one variable for dislocation density indicating the site energy, and the last variable for color showing various grains. It should be mentioned that the orientation is randomly determined to be between 0° and 180°. To simplify the CA model, the primary dislocation density of grains is uniform which enhances with improved deformation, the nucleation of dynamic recrystallization happens only on grain boundaries, and no dislocation gradient occurs from the center to the boundary [44]. The schematic of different steps of the CA method regarding the dynamic recrystallization (DRX) during severe plastic deformation is shown in Fig. 5. In the first step, the primary grain is produced by running the incipient structure generation of CA depending on the state transition rules. Then, the time step is calculated by Eq. (27) in the second step. In the third step, the dislocation density increment along with the deformation is calculated by Eq. (10). After recrystallization in a special cell, the density of the cell is considered as ρ_{initial} in the CA model. In the last step, the growth of the recrystallized nuclei with respect to the recrystallized cells is considered [34]. Figure 6 summarizes the simulation structure.

2.5 Finite element analysis of vibration influence during FSW

Vibration energy in FSW plays two significant effects on the FSW process: One is the softening due to the interaction between plastic deformed materials and vibration energy. This interaction would influence the evolution of dislocation and consequently decrease the flow stress of the plastically deformed materials [27]. The other factor is the preheating because the vibration friction heat stems from the relative movement. Both the preheating and softening effects can influence the heat production and plastic material flow, which consequently influence the joining process and the final characteristics of jointed parts. Equation (28) indicates a non-dimensional stress ratio ($\Delta\lambda$) in accordance with the thermal activation hypothesis which was verified by the vibration energy density [45]:

$$\Delta\lambda = \frac{\tau_{\text{v}} - \tau_0}{\tau} = -\beta'\left(\frac{E}{\hat{\tau}}\right)^{m'} \tag{28}$$

where τ_0 indicates the shear stress during the conventional process, τ_{v} indicates the shear stress with vibration at the similar condition, $\hat{\tau}$ indicates the mechanical threshold shear stress, E indicates the vibration energy density, and β' is a parameter estimated by comparison of the predicted flow stress with the experimentally examined amplitude for acceptable agreements. From the load–displacement curves, the flow stress is evaluated during vibration that accompanied the hot upsetting of AZ91 magnesium alloy, and m' is the factor to be achieved by actual testing which may change from 0.5 to 1, based on the relationships in literature [45].

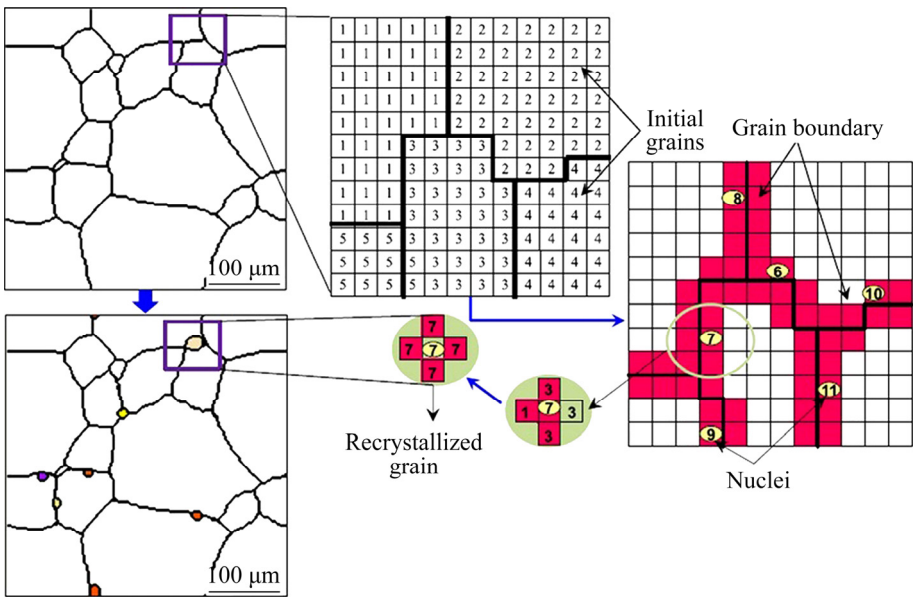

Fig. 5 Schematic of dynamic recrystallization in cellular automaton model [34]

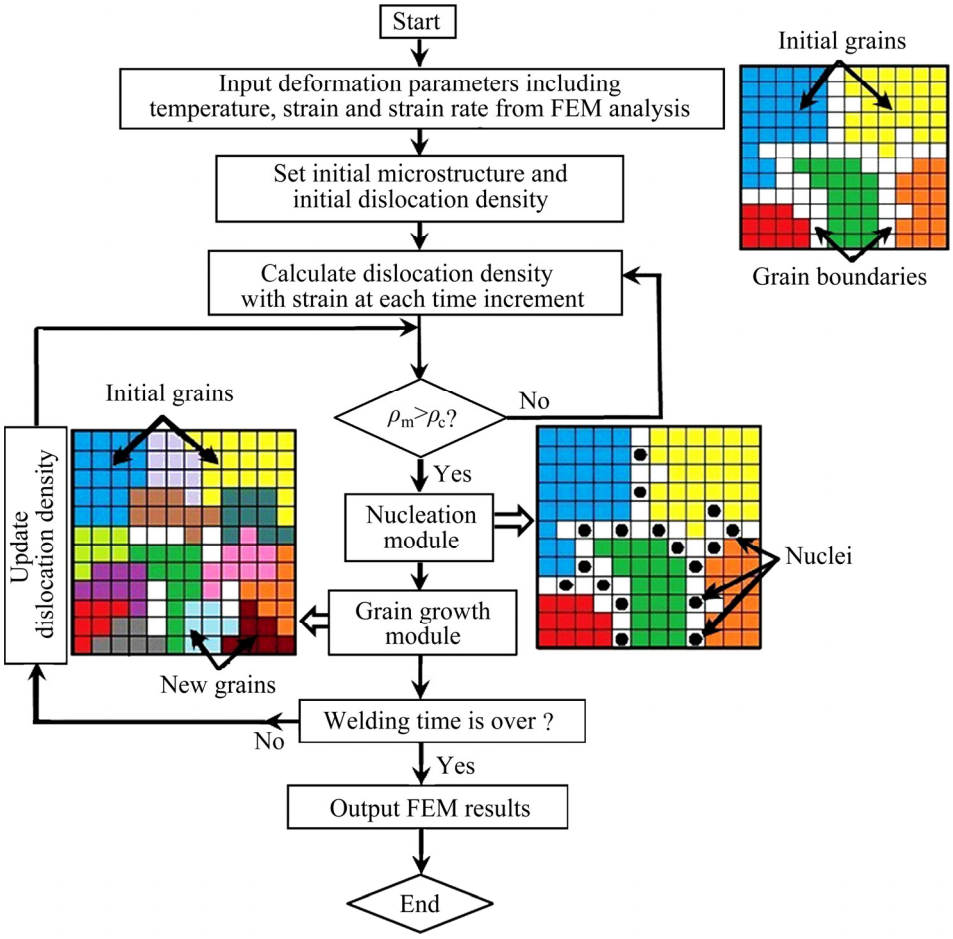

Fig. 6 Flowchart of CA model for DRX

The relationship between the single crystal shear stress (τ') and the polycrystal uniaxial stress (σ') was presented by Taylor factor (M'):

$$M'=\sigma'/\tau' \tag{29}$$

The vibration reflection initially affects the dislocation motion, so the thermal ingredient of the flow stress is varied [46]. Equation (30) indicates the thermal ingredient of flow stress which was developed by the vibration energy density:

$$\frac{\sigma_{\text{th}}-\sigma_{\text{th},v}}{\hat{\sigma}_{\text{th}}}=\beta'\left(\frac{M'E}{\hat{\sigma}_{\text{th}}}\right)^{m'} \tag{30}$$

According to Eq. (30), $\hat{\sigma}_{\text{th}}$ indicates the thermal ingredient of flow stress as vibration is applied. It is worth mentioning that the thermal ingredient of flow stress based on average velocity (v_{d}) of a movable dislocation is given as [47]

$$\sigma_{\text{th},v}=\hat{\sigma}_{\text{th}}\left[1-\left(\frac{k_{\text{B}}T}{g_0\mu_{\text{m}}b^3}\ln\left(\frac{\dot{\varepsilon}_0}{\dot{\varepsilon}_{\text{v}}}\right)\right)^{1/q}\right]^{1/p} \tag{31}$$

where p and q indicate the shape of hindrances ($0<p\leq1$, $1\leq q\leq2$), g_0 indicates a pre-index, μ_{m} indicates the shear modulus according to various temperatures, and $\dot{\varepsilon}_{\text{v}}$ indicates the strain rate as vibration is applied. By considering the thermal ingredient of flow stress with and without vibration into Eq. (30), the following equation will be achieved:

$$1-\beta'\left(\frac{M'E}{\hat{\sigma}_{\text{th}}}\right)^{m'}=\left[1-\left(\frac{k_{\text{B}}T}{g_0\mu_{\text{m}}b^3}\ln\left(\frac{\dot{\varepsilon}_0}{\dot{\varepsilon}_v}\right)\right)^{1/q}\right]^{1/p} \tag{32}$$

To improve the calculation, p and q have been determined to be an amplitude of 1 (this amount ($p=q=1$) has been generally applied to magnesium alloys). Therefore, Eq. (32) can be considered as a fundamental equation to calculate the strain rate for both conditions:

$$\frac{\dot{\varepsilon}_{\text{v}}}{\dot{\varepsilon}}=\exp\left[\frac{-g_0\mu_{\text{m}}b^3\beta'}{k_{\text{B}}T}\left(\frac{M'E}{\hat{\sigma}_{\text{th}}}\right)^{m'}\right] \tag{33}$$

Zener–Holloman factor following vibration

would be given as

$$Z_{\mathrm{v}}=\dot{\varepsilon}_{\mathrm{v}}\exp\left(\frac{Q}{RT}\right) \tag{34}$$

Replacing Eq. (33) into Eq. (34), we achieve

$$Z_{\mathrm{v}}=\dot{\varepsilon}\exp\left[\frac{Q}{RT}-\frac{g_0\mu_{\mathrm{m}}b^3\beta'}{k_{\mathrm{B}}T}\left(\frac{M'E}{\hat{\sigma}_{\mathrm{th}}}\right)^{m'}\right] \tag{35}$$

Equation (36) indicates the Zener–Holloman factor and vibration:

$$Z_{\mathrm{v}}=A(\sinh(\alpha\sigma_{\mathrm{v}}))^n \tag{36}$$

Replacing Eq. (36) into Eq. (35), we achieve

$$A(\sinh(\alpha\sigma_{\mathrm{v}}))^n=\dot{\varepsilon}\exp\left[\frac{Q}{RT}-\frac{g_0\mu_{\mathrm{m}}b^3\beta'}{k_{\mathrm{B}}T}\left(\frac{M'E}{\hat{\sigma}_{\mathrm{th}}}\right)^{m'}\right] \tag{37}$$

The stress with vibration by adopting the representation of the hyperbolic sine behavior and using Eq. (36) will be displayed as [47]

$$\sigma_{\mathrm{v}}=\frac{1}{\alpha}\ln\left\{\left[\frac{\dot{\varepsilon}}{A}\exp\left(\frac{Q_{\mathrm{v}}}{RT}\right)\right]^{1/n}+\left[1+\left[\frac{\dot{\varepsilon}}{A}\exp\left(\frac{Q_{\mathrm{v}}}{RT}\right)^{2/n}\right]\right]^{1/2}\right\} \tag{38}$$

where Q_{v} is the activation energy during vibration and is defined as

$$Q_{\mathrm{v}}=Q-\frac{g_0\mu_{\mathrm{m}}b^3\beta'R}{k_\beta}\left(\frac{M'E}{\hat{\sigma}_{\mathrm{th}}}\right)^{m'} \tag{39}$$

To decrease the energy barrier with respect to the dislocation movement which leads to better mobile dislocation and higher average speed of the mobile dislocation, the superimposed vibration energy has been used. The vibration energy density (E) is evaluated according to [47]

$$E=4f_{\mathrm{v}}^2\pi^2\xi^2 \tag{40}$$

where f_{v} indicates the frequency and ξ indicates the amplitude of the used vibration during the process. Table 5 presents the typical parameters and their amplitudes utilized in the constitutive equation. Mentioned equations are the modified constitutive equation including the vibration effect that incorporates the influences of process parameters namely temperature, strain rate, material properties such as shear modulus, and vibration energy density.

Table 5 Values of parameters applied in calculation

Parameter	Value
Pre-factor, g_0	0.22
Taylor factor, M'	3.2
Coefficient in Eq. (28), m'	1.0
Coefficient in Eq. (28), β'	65
Coefficient in Eq. (36), n	3.5
Vibration frequency, f_{v}/Hz	38
Vibration amplitude, ξ/mm	0.6

3 Results and discussion

3.1 Modeling validation

Figures 7 and 8 show the temperature history and axial force distribution for experimental and simulation analyses of AZ91 alloy during FSW and FSVW, respectively. An acceptable agreement

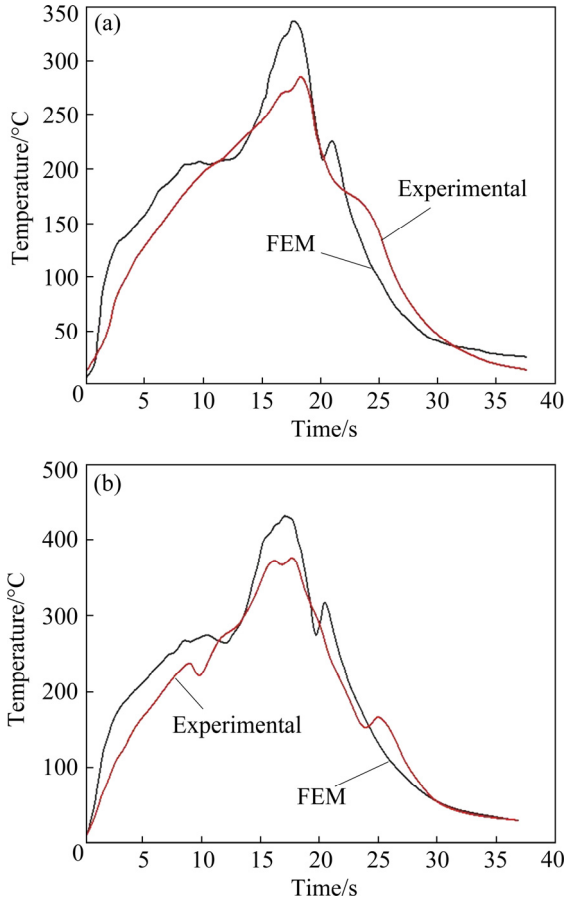

Fig. 7 Comparison of thermal analysis between experimental and simulation results of AZ91 alloy during FSW (a) and FSVW (b)

between the FEM and empirical measurements is observed. The temperature peak in FSVW is higher than that in FSW because of the vibration effect on introducing higher heat input into the weldment during the joining process [14]. That is to say, the relative mobility between the welding tool and material during the FSVW yields higher strain rates, therefore yielding more plastic deformation and heat generation. The average axial force during FSVW is lower compared to the FSW, which can be attributed to the additional softening of the sample in the presence of vibration [26].

3.2 Thermal, strain rate, dislocation, and material flow analysis

The measured temperature fields of both FSW-ed and FSVW-ed samples are presented in Fig. 9. The temperature profile is almost symmetric with respect to the joint line due to the dominant role of rotational speed compared to the traverse speed on heat generation during the welding process. And also the maximum temperature values display at the contact areas of the tool and workpiece plate owing to a great deal of plastic deformation while the minimum temperature values are observed far away from the joining tool. The temperature gradient, during the welding process, is not the same behind and forward the joining tool, and therefore the shapes of thermal contours are akin to ellipses. Furthermore, the contour for FSV joint specimen is larger in comparison to the FS welded specimen; additionally, the temperature profile around the welding position for the former sample is higher compared to the latter sample. Both results are considered to be related to the weldment vibration during FSVW. Weldment vibration improves the area in which the tool influences and consequently, the higher volume of

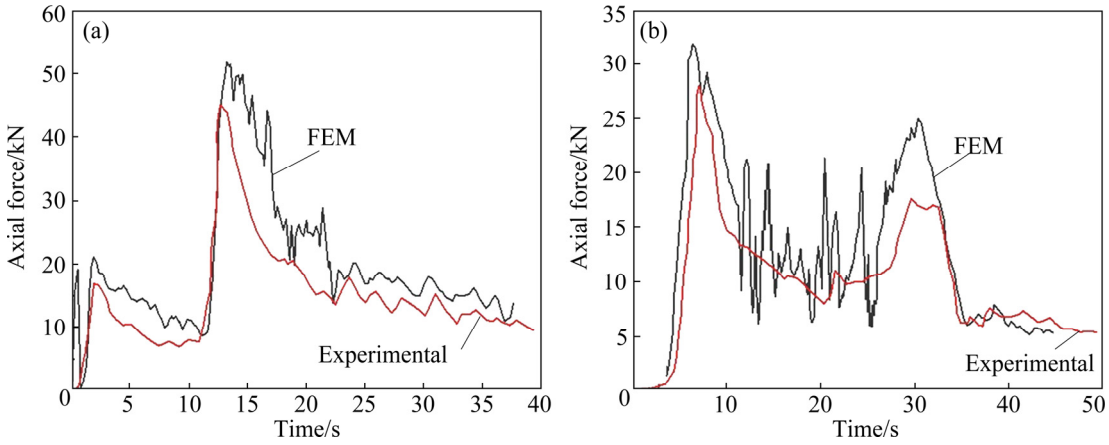

Fig. 8 Variation in axial force during FSW (a) and FSVW (b) in experimental and simulation measurements

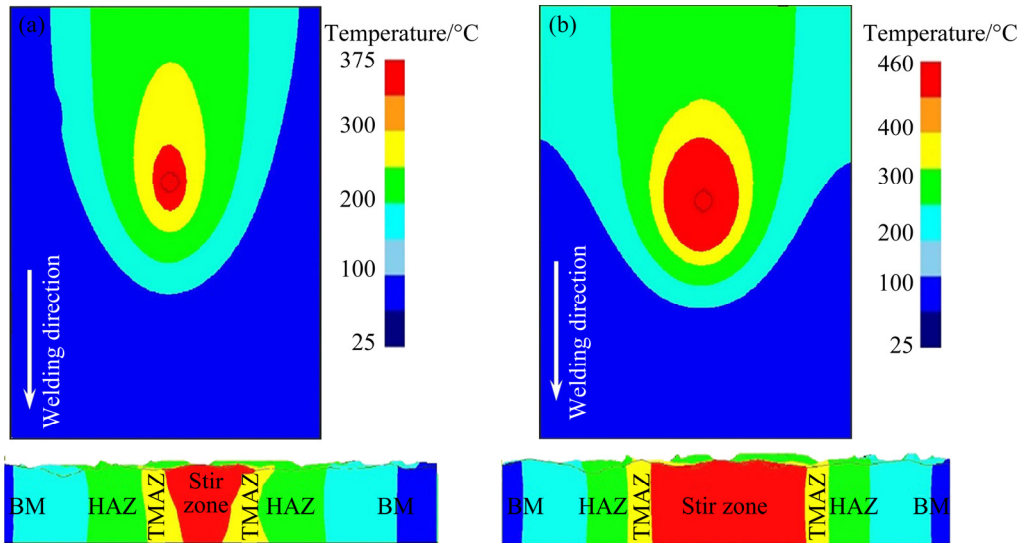

Fig. 9 Top and cross-section views of temperature profile in joint zone: (a) FSW; (b) FSVW

metal is deformed. Weldment vibration also enhances the material deformation into the stir zone (SZ) and causes the high-velocity pattern of various points [48]. Therefore, the massive plastic and heat deformation causes a higher temperature in the weld zone side next to the center.

Simulation data in strain history around the joint position for FSW and FSVW methods are revealed in Fig. 10. It is seen that the strain rate profile unlike the temperature profile is almost asymmetric, that is, the plastic deformation is influenced by combination of rotational and traverse speeds of welding tool for both welding conditions. Besides, some of the materials of the workpiece are expanded toward the advancing side and can cluster at this side on the top surface. This event matches well with the phenomenon of asymmetrical deformation on the cross-section. And also its maximum peak is biased toward the stir zone (SZ) due to a positive combination of rotational and traverse speeds on higher plastic deformation. The strain rate because of an increase in plastic deformation and frictional heat increases and in the joining phase remains almost unchanged. Figure 10 indicates that the strain profile with respect to the FSVW process is higher in comparison to the FSW process due to high sliding between welding tool and material in the weld area. Based on Fig. 10, the highest strain distribution for FSVW is around 24.6 while it is around16.8 for FSW. What is more, the plastically deformed zone improves with the introduction of vibration during the joining process. This is related to the fact that the vibration causes a more upsetting impact on the weldment and consequently, generates a deeper and wider deformed area compared to the welding condition without using vibration.

Figure 11 compares the distribution of dislocation density in 300×300 cells for both FSW and FSVW conditions. It is evident that the dislocation density during FSVW is higher than that of the FSW process due to the influence of vibration. It has been accepted that the dislocation density depends on strain and strain rate during the severe plastic deformation [49]. A higher dislocation density leads to passing the critical value in a short time, and the DRX initiates during FSVW. From the other sides, the driving force with respect to grain growth decreases as the dislocation density improves. In addition, the boundaries of the DRX grains can be considered again as nucleation sites as their dislocation density is enough for nucleation. The discrepancy in the dislocation density gives rise to the improvement in toughness and ductility of the material.

FE results in material flow during FSW and FSVW processes are displayed in Fig. 12. These contours are related to the material flow of the workpiece in the surface just beneath the shoulder and around the joint position. The outer circle denotes the shoulder diameter and the inner circle denotes the pin diameter. The flow paths of materials show that the severe material flow fundamentally happens at the tool shoulder contact

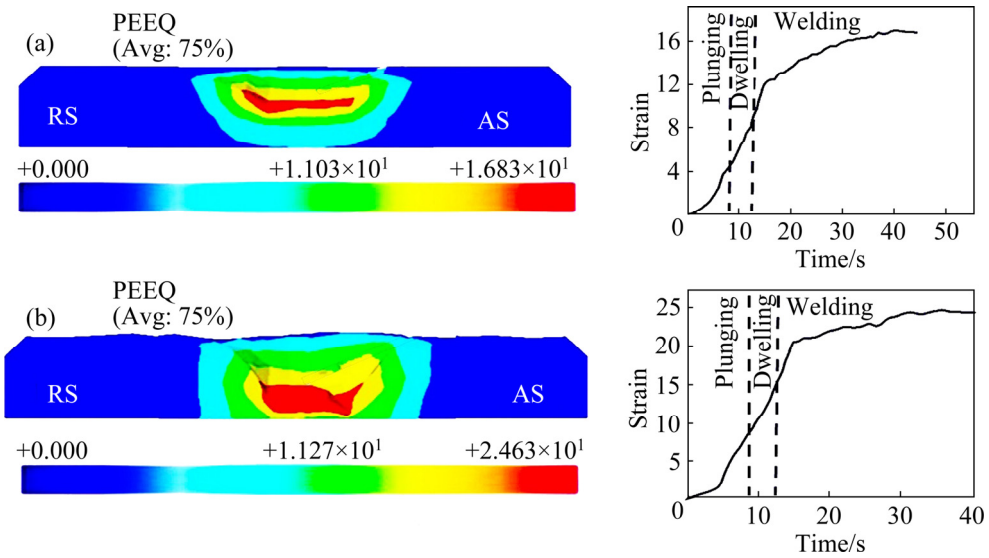

Fig. 10 Cross-section and value variation of strain profile surrounding joint position for FSW-ed (a) and FSVW-ed (b) samples

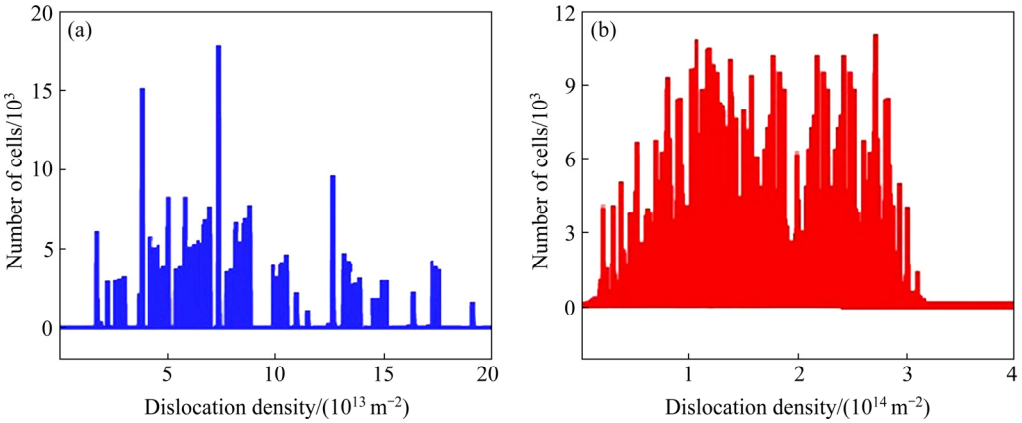

Fig. 11 Comparison of distribution of dislocation density during different joining processes: (a) FSW; (b) FSVW

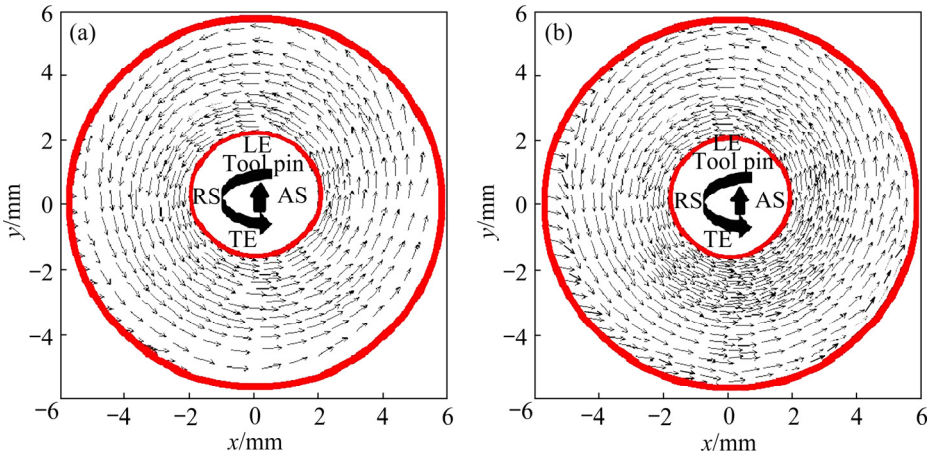

Fig. 12 FE results about material flow of workpiece in surface just beneath shoulder in FSW (a) and FSVW (b) processes (TE−Trailing edge; LE−Leading edge)

surface. The flow of material during the FSW process is attributed to the high-speed rotating shoulder from the advancing side to the retreating side and finally backward to the joint line. From Fig. 12, the flow arrows are almost symmetric in the vicinity of the welding tool pin although the asymmetry in the flow patterns is anticipated because of the combined effect of traversing and rotation of the welding tool pin. It is obtained that flow arrows in FSV welded sample are denser than those in FS welded specimen. This can be attributed to sample vibration as well as tool rotation and transverse movements during the FSVW process which enhances the material flow. Based on Fig. 9, a higher temperature around the joint position is predicted for FSVW with respect to FSW. Higher temperature causes higher softening of material around the tool and consequently, more deformation of material occurs [50]. Therefore, it can be said that higher shearing of material is performed in the FSV welded sample than in the conventional FS welded sample.

Figure 13 displays the velocity variation in the stir zone for both welding conditions at the same location. It is clear that the velocity value in the AS is higher compared to the RS. This can be associated with higher heat flux and shear stress on AS with respect to the RS. In addition, the velocity contour during the FSVW is higher than that during the conventional FSW process. The maximum flow velocity depends on various factors such as the traverse and rotational speeds of the tool pin, slipping condition between tool and the material, surface characteristics of the joining tool and the kind of joint materials, as indicated from the previous investigations [51−53]. The authors believe that vibration causes a reduction in the interfacial forces and improves the material flow velocity in the stir zone. This result validates the results obtained by ZHAO et al [29]. They applied the ultrasonic vibration during the FSW process to analyze the velocity variation between the welding

tool and weldment material. It was shown that the velocity distribution under the tool shoulder and next to the pin surface has been improved as the ultrasonic vibration is applied.

3.3 Microstructure evolution

It has been known that various factors such as temperature, strain, and strain rate, have affected the microstructure evolution during the FSW process [54−56]. However, the discrepancy in nucleation rate resulted from temperature during the nucleation period is negligible, due to the fact that the temperature variation is small compared to the maximum temperature, and thus only the temperature affecting grain growth is estimated in the FSW process. When the strain rate is high, the accumulation of dislocation is fast, recrystallization nucleation is more obvious to happen, the period of recrystallization nucleation is short, the number of recently formed crystal grains is high, and the time for recrystallization crystal nuclei to grow is short. During the FSW process, DRX causes the production of fine equiaxed grains in the stir zone (SZ). Figure 14 displays the microstructure of parent metal obtained by experimental techniques and FE analyses, and also presents the graphical distribution of a number of grains with respect to grain size. Based on this graph, the average grain size is about 148 μm. This is in high-grade agreement with the experimental measurements which indicated that the average grain size is about 133 μm (Fig. 14(c)). This discrepancy between experimental and numerical values can be associated with the effect of precipitation phases that were not considered in the numerical study during the welding process.

Figure 15 displays the distribution of grain size obtained using the cellular automation step (CAS) for FSW and FSVW processes. It is evident that the grain size shows no variation at the beginning step of analysis for both FSW and FSVW conditions. By increasing the CAS, the grain size experiences normal distribution during the processes. And also, it is obtained that the distribution of grain size shows a time-invariable tendency with respect to normal grain growth. The maximum frequency is at R/R_m=0.8, that is, the size of grains is nearly equal to the average size in the microstructure, while for

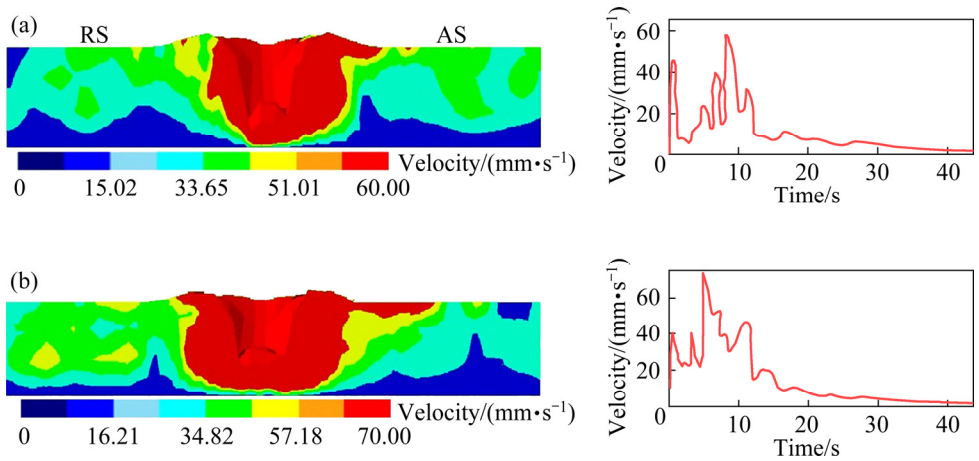

Fig. 13 Velocity contour and value in weld area for different welding processes: (a) FSW; (b) FSVW

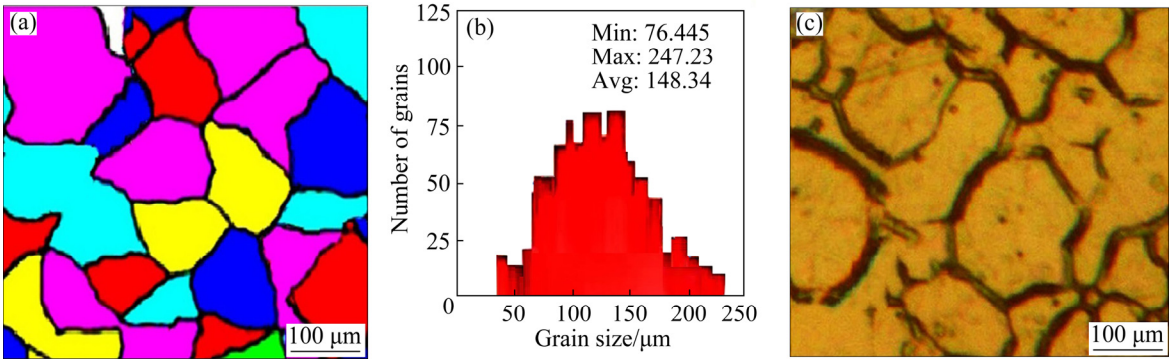

Fig. 14 Comparison between FEM outcomes (a, b) and experimental data (c) of base metal microstructure

lower frequency, the R/R_m shows to be zero. It is indicated that there is a need for time-dependent deformation to start DRX. It is also observed that the vibration effect can decrease the incubation period due to the rate of dislocation accumulation and also the critical strain. That is to say, the rate of dislocation accumulation increases, and the critical strain decreases as vibration is applied during the welding process.

Figure 16 presents the microstructure of different areas of the weld during FSW and FSVW. Grains in the stir zone (SZ), because of the improvement of DRX, are finer than grains in TMAZ and HAZ. Moreover, the grains of the FSV welded samples (in all areas of the joint zone) are smaller than grains of the FS welded samples. The experimental results show that SZ grains for FSV welded samples ((14.43±2) μm) were finer than those for FS welded samples ((23.43±2) μm). This can be attributed to the weldment vibration in FSVW. The vibration of the sample, besides the stirring and also traversing movements of the welding tool, enhances metal deformation in FSVW [57]. Metal deformation, which is revealed by strain (ε), is associated with flow stress (σ) ($\sigma=k\varepsilon^n$), and the flow stress improves as the strain raises. It is well-known that material deformation (strain) has a direct relationship with the density of

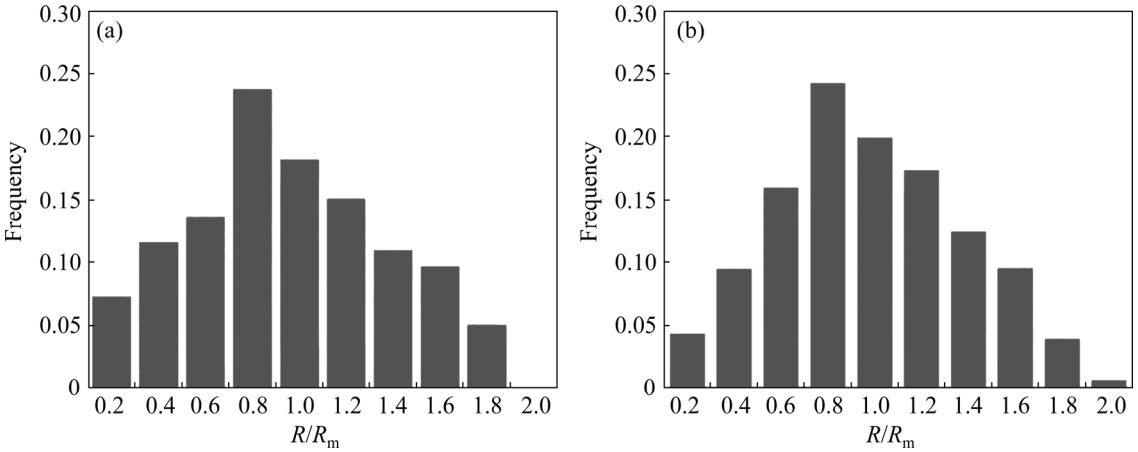

Fig. 15 Distribution of grain size at different cellular automation steps (CAS): (a) FSW; (b) FSVW

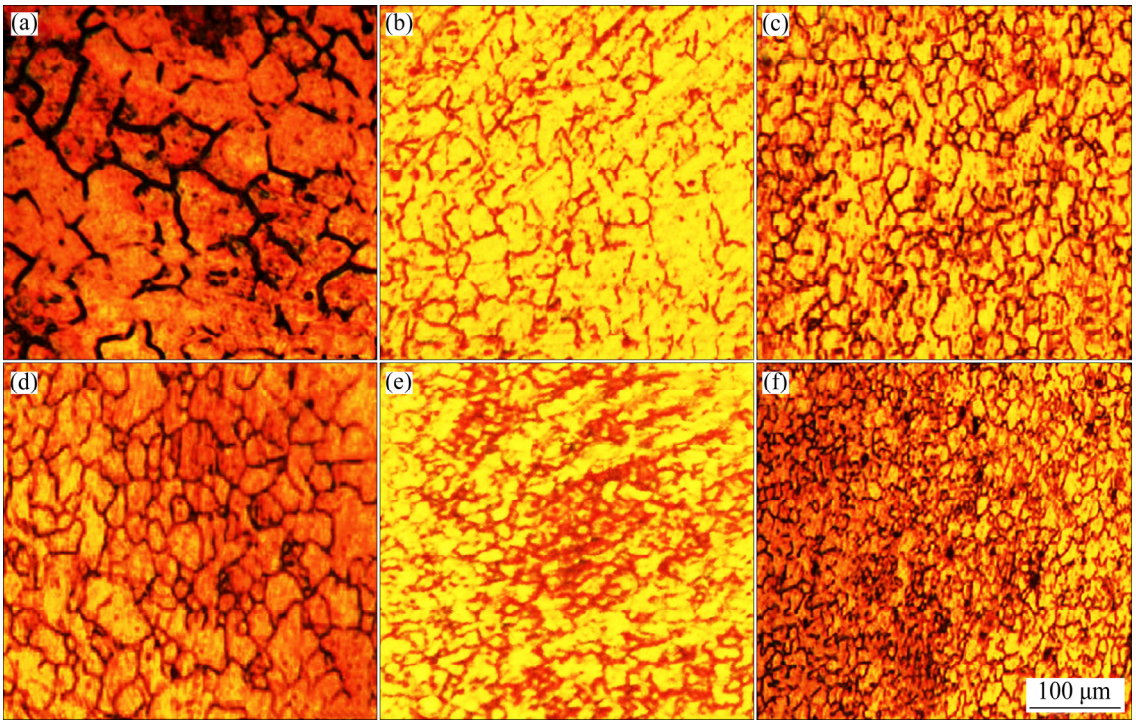

Fig. 16 Different regions of weld zone through FSW (a−c) and FSVW (d−f): (a, d) HAZ; (b, e) TMAZ; (c, f) SZ

dislocations [57,58]. The rapid increase of dislocations and also continuous improvement in dislocation density happen with developing strain. By increasing the dislocation density, dynamic recovery (DR) enhances, and so grain modification increases [59]. On the other hand, in terms of the Zener−Holloman (Z) parameter during the thermomechanical process [60], there is

$$d = a'Z^{b'},\ Z = \dot{\varepsilon}\exp(\frac{Q}{RT}) \Rightarrow$$
$$\ln d = \ln a' + b'\ln\left(\dot{\varepsilon}\exp\left(\frac{Q}{RT}\right)\right) \quad (41)$$

A higher strain rate during the FSVW (based on Fig. 10) in comparison to the FSW process leads to higher Z and finer grains develop. In Eq. (41), $\dot{\varepsilon}$ indicates the strain rate, and a' and b' are the constants. Based on Figs. 9−13, the thermal and also softening effects of vibration cause the plastic deformation to occur earlier, so that the dislocation achieves earlier, and as a result, the recrystallization nucleation process begins earlier. According to Eq. (42), during the FSW, the rate of nucleation is dependent on temperature and strain rate [37]:

$$P_{\text{nucl}} = D\dot{\bar{\varepsilon}}\exp\left(-\frac{Q}{RT_{\text{abs}}}\right) \quad (42)$$

where D is the ratio constant (e.g. 10^3 for lightweight alloys), and $\dot{\bar{\varepsilon}}$ defines the maximum value of the equivalent strain rate. By using vibration during FSW, the material deformation enhances and consequently, more strain rate is generated in the weld zone [60]. Therefore, the number of retained grains reduces, and the size of retained grains decreases. This means that, the holding time of high temperature after nucleation, during the FSVW, becomes shorter, and the growth of recrystallized crystal grains is limited and as a result, the final average grain size decreases. Another effective reason can be associated with the effect of the Zener pinning in grain growth. During the Zener pinning, second-phase particles impede the growth of grains and postpone the coarsening of matrix phase grains by pinning the movement of grain boundaries. The grain boundaries are the main source of dislocations [61]. The higher number of dislocations in FSV welded samples in comparison to conventionally FS-welded samples leads to higher interaction of dislocations during severe plastic deformation.

For the ability of the cellular automaton (CA) method to analyze the dynamic recrystallization (RDX) process and microstructure evolution for both FSW and FSVW, the real experimental conditions were considered in the Deform-3D software. Figures 17 and 18 show the different areas of the welded zones simulated for FSW and FSVW processes, respectively, under the same welding condition to show different steps of the recrystallization process. According to Figs. 17(a) and 18(a), plenty of nuclei were nucleated at random places in grain boundaries at the initial step. Then, according to the method provided by CHEN et al [62], the nuclei have an equiaxial growth into the matrix as shown in Figs. 17(b) and 18(b). The grains grow until they impinge on each other. A new turn of nucleation was introduced when previous nuclei had grown into a particular percentage of the entire microstructure (Figs. 17(c) and 18(c)). After impinging with other grains, the growth of grains stops, and after numerous steps of the nucleation and growth, the final microstructure is generated. According to this process, primary microstructures with various grain sizes and distributions can be obtained. Based on the dislocation accumulation map (density dislocation map) of each area, white points generate within the dark zones by nucleation and growth and start to consume them. Hence, the dark areas gradually decrease explaining the decrease of dislocation density. Based on these results, the process of nucleation and grain growth is quicker for samples during FSVW compared to FSW. To be more specific, the number of subgrains in the sample produced by FSVW is fewer and larger compared with the grains during conventional FSW in the first step of welding. In this condition, subgrains formed into grain interiors reduce, and some recrystallized grains are produced at the grain boundaries. As the process continues, a large number of fine grains are formed at the grain boundaries and only a few subgrains develop into grain interiors. This can be associated with the vibration effect on grain modification during severe plastic deformation. During the vibration, the matrix is completely recrystallized and the nucleation rate is much higher than the growth rate of grains, so the new nuclei have no enough space and time to grow before the next cycle of nucleation at both recrystallized grain (R-grain) and un-crystallized grain boundaries.

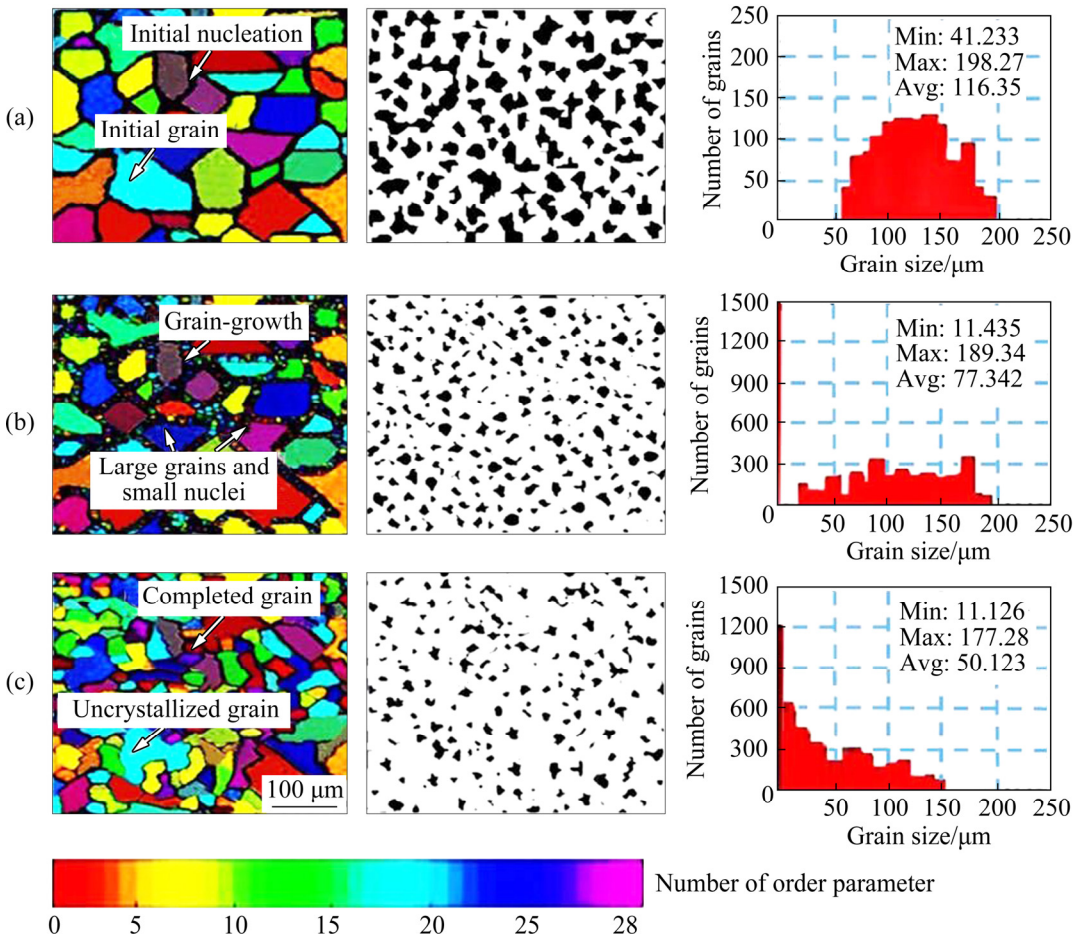

Fig. 17 Simulation of multi-step nucleation and grain growth of weld sample during FSW: (a) Nucleation; (b) Grain-growth; (c) Completed grain

Therefore, the size of R-grains is smaller for FSVW in comparison to that for conventional FSW. In addition, based on growth velocity and grain boundary energy as indicated in Eqs. (19) and (26), respectively, enough recrystallization temperature and large stored energy during the FSVW process lead to a high rate of nucleation and grain growth. This phenomenon leads to the completion of the recrystallization process for a short time, and consequently, the microstructure experiences more refinement conditions.

3.4 Impact of vibration frequency

The influence of vibration frequency on the strain distribution (volume-averaged equivalent plastic strain (PEEQVAVG)) during the welding process is presented in Fig. 19. According to the displayed results, the strain rate values increase as vibration frequency increases. The highest strain value for the frequency of 50 Hz is around 60 while it is about 17 for a vibration frequency of 32 Hz. This can be attributed to higher deformation of the material in the stir zone as vibration enhances; therefore, higher deformation of the material leads to higher strains in the material and more enhanced DRX happens. In other words, high vibration values decrease the viscosity and flow stress in the stir zone, so the flow of material in this area improves and results in an improvement in the strain rate and flow speed. This result is a vital factor to have a sound and modified microstructure, which in turn improves the mechanical performances of the weld.

To verify the influence of vibration frequency on grain size during simulation analysis, a comparison between experimental and simulated grain size in the stir zone for different vibration frequencies was carried out. The stir zone was determined for the microstructure analyses because the grain modification in this zone is clearly identified. Figure 20 displays the grains in the stir

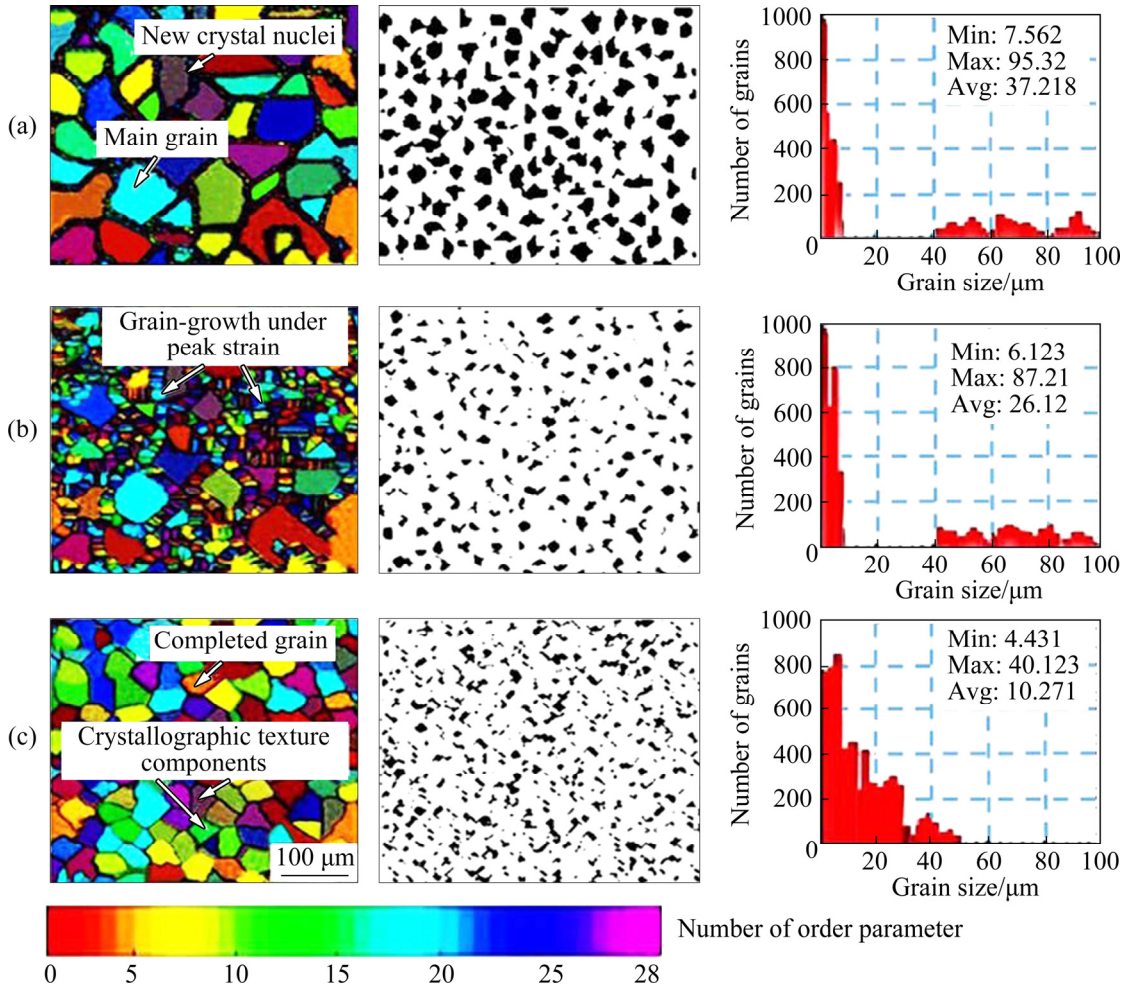

Fig. 18 Simulation of multi-step nucleation and grain growth of weld sample during FSVW: (a) Nucleation; (b) Grain-growth; (c) Completed grain

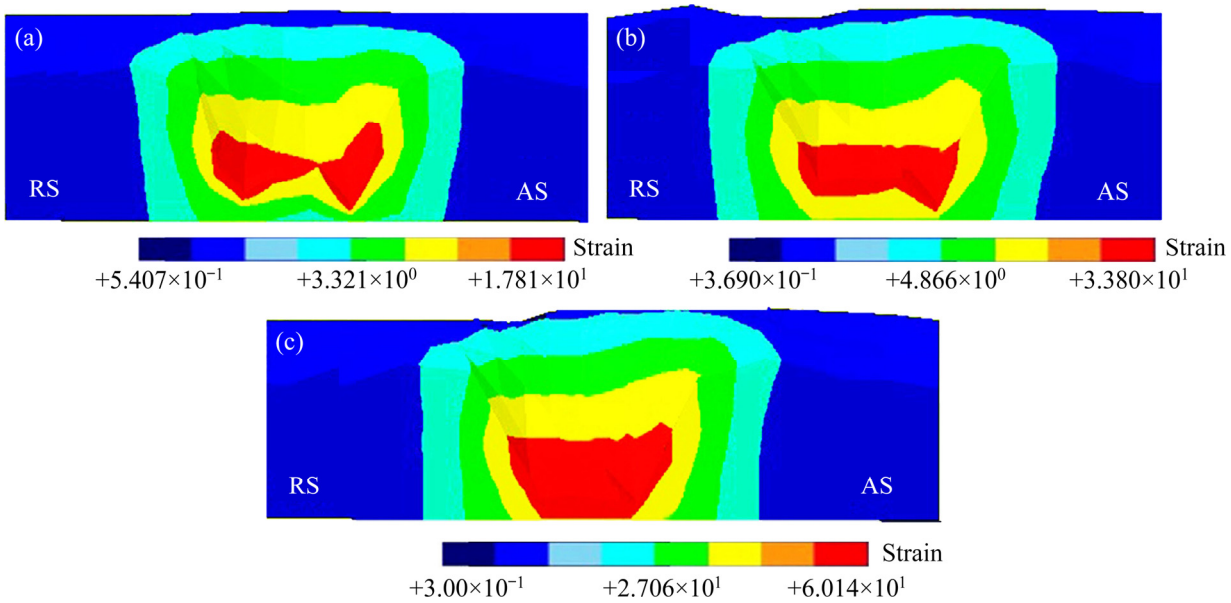

Fig. 19 Strain distribution profiles for different samples under different vibration frequencies during FSVW: (a) 32 Hz; (b) 42 Hz; (c) 50 Hz

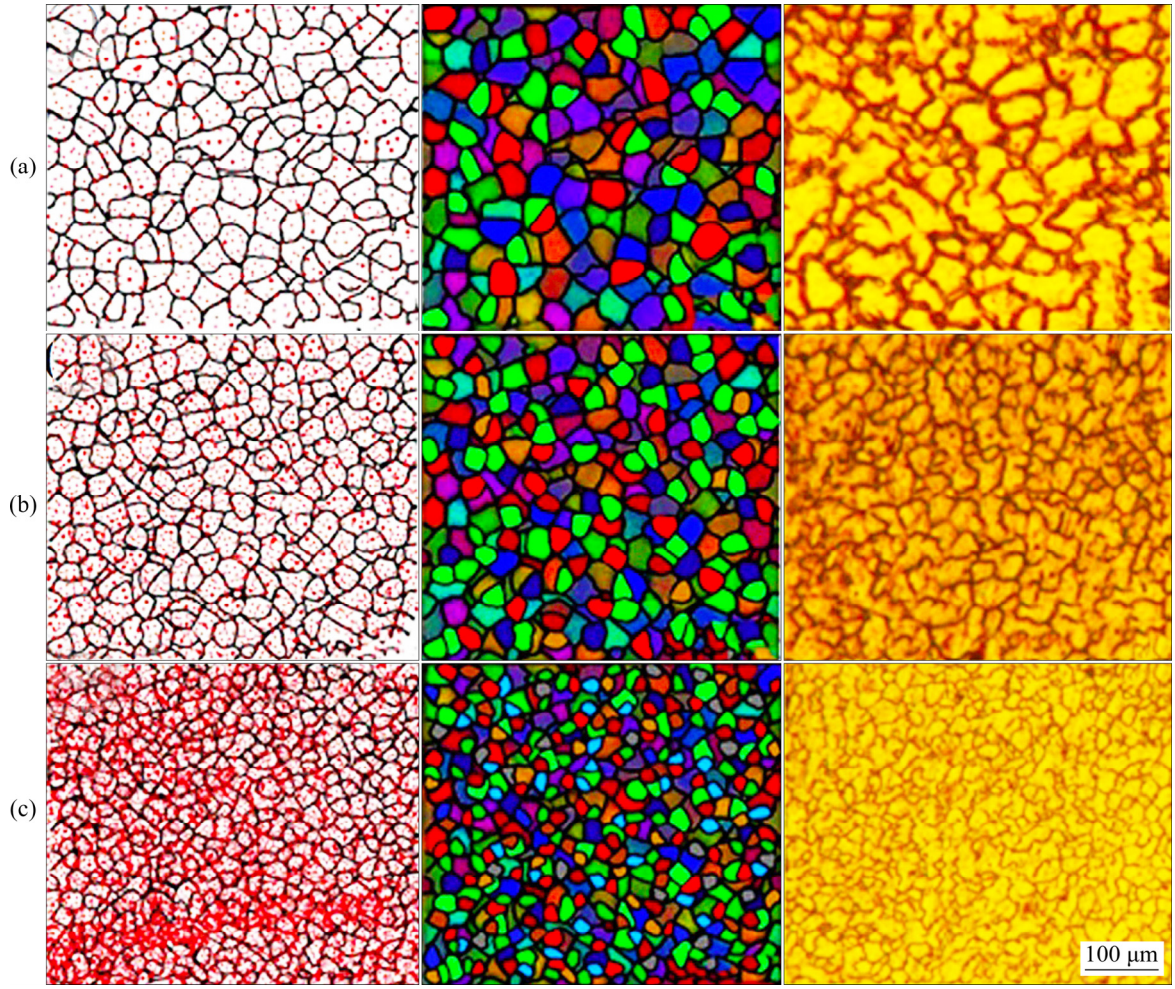

Fig. 20 Grain size distribution and recrystallization process in different stir zones under different vibration frequencies during FSVW: (a) 32 Hz; (b) 42 Hz; (c) 50 Hz

zone (SZ) for three vibration frequencies (32, 42 and 50 Hz), under experimental and FEM studies. There is an excellent agreement in terms of both the grain size distribution and topography between experimental and CA simulation data. Based on the nucleation map in different sites of the stir zone (SZ) for various joining processes, it is indicated that the new grains nucleate from the previous grain boundaries and then begin to grow. In fact, the nucleation of new grains happens in the preferential sites, and then, because of the presence of sufficient heat and also the dislocation density discrepancy, the grain growth starts and keeps going as far as the driving force with respect to boundary migration is positive. It is illustrated that in the stir zone for sites with lower stored energy, nuclei nearly occur on the grain boundaries (GB). However, by increasing stored energy due to increasing vibration frequency, more plastic deformations occur, and consequently, stored energy inside the grains is high, sufficient to improve nucleation inside the grains. In other words, the recrystallized grains primary nucleate at the grain boundaries of the deformed grains in the primary microstructure with respect to a specific plastic deformation degree. By increasing the plastic strain, these grains grow. With the improvement of the plastic deformation process, the recrystallized grains cease growing and experience plastic deformation. Consequently, new crystal nuclei are generated at the grain boundaries of the earlier generated recrystallized grains [63]. It is seen from Fig. 20 that grain size decreases as vibration frequency enhances. Changing colors of the grains indicate various crystal orientations of the dynamic recrystallization grains while the black lines denote grain boundaries with a misorientation angle higher than 15° between grains. It is worth noting that the DRX process occurs when special

energy conditions are fulfilled. The debut of DRX is dependent on the density of the dislocations during plastic deformation. By increasing the dislocations of the deformed material and the access to the critical strain during welding, the DRX nuclei will generate at its primary grain boundary. Then, the completed evolution of dynamic recrystallization happens as the steady-state flow is achieved, and full DRX grains can maintain the equiaxed shape and fixed size. Therefore, the higher deformation and strain in the SZ due to increasing vibration frequency lead to larger strain and dislocation density during the FSVW. More dynamic recrystallization happens, and as a result, grains experience large refinement. These results are in reasonable agreement with Eq. (5).

The influence of deformation vibration on the average grain size is displayed in Table 6. It is evident that the grain size of the stir zone reduces with increasing the vibration frequency. Vibration fundamentally influences the DRX process by increasing the density of dislocations. The more the dynamic recrystallization is, the more the grain refinement is.

Table 6 Influence of vibration frequency on mean grain size

Vibration frequency/Hz	Number of residual large-size grains	Size of most grains/μm	Average grain size/μm
32	<12	11	13
42	<6	5.5	7
50	<4	2−3	5

Figure 21 compares the incubation period and percentage over the whole plastic deformation during the FSVW for various vibration frequencies. It is indicated that the incubation period and percentage decrease as vibration frequency improves. This can be associated with the influence of vibration softening to increase strain rate and dislocation accumulation by increasing the vibration frequency, and as a result, the incubation period is decreased. It should be mentioned that there is a competition between the effect of preheating with strain rate and dislocation density as vibration increases. According to the results in Fig. 22, the effect of strain rate and dislocation density is dominated with respect to the effect of preheating. This result verifies the obtained outcome reported by HU et al [64]. They showed that the subgrain mobility increases because of the high vacancies implemented by ultrasonic vibration during FSW, and thus the normalized nucleation criterion decreases and a large number of nuclei contribute in dynamic recrystallization. Consequently, the growth rate of subgrains is improved due to the excess vacancies and the nucleation rate of dynamic recrystallization during the FSVW process is improved.

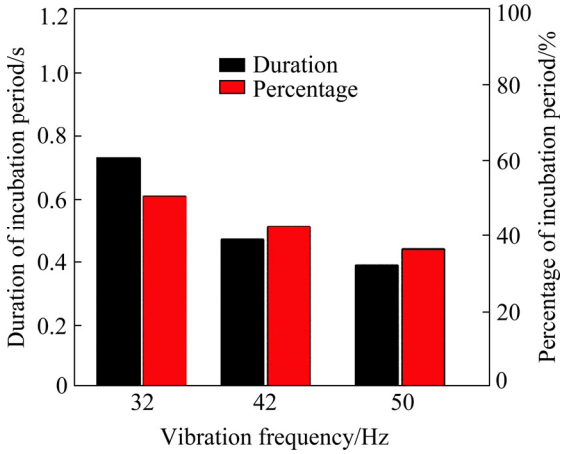

Fig. 21 Period and percentage of incubation during FSVW process under different vibration frequencies

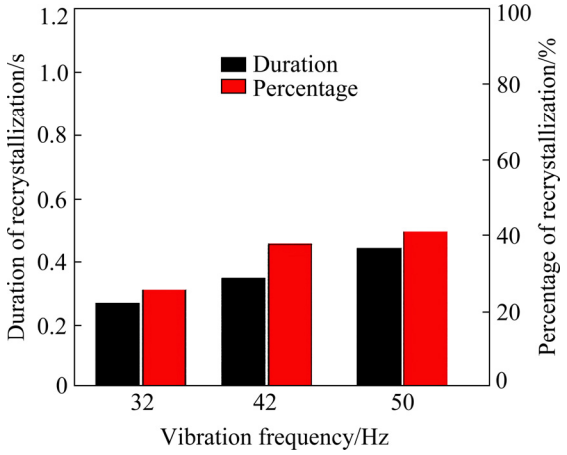

Fig. 22 Period and percentage of recrystallization during FSVW process under different vibration frequencies

According to Fig. 22, the period and percentage of recrystallization during the FSVW process increase as vibration frequency improves. As the vibration frequency develops, the recrystallization period improves because the duration of the high strain rate becomes larger because of the development of material flow around the welding tool. And also, the recrystallization percentage increases because the accumulation of

dislocations occurs faster, so the nucleation process starts earlier and finishes later as vibration frequency increases.

4 Conclusions

(1) The temperature and strain in FSV welded samples are higher than those in FS welded specimens.

(2) The analytical results about the microstructure of the weld zone (namely, SZ, TMAZ, and HAZ) have good compatibility with results from the experiments. The grain size of the weld area decreases as vibration is applied during friction stir welding.

(3) Workpiece vibration in FSVW results in higher deformation of material compared to material deformation in FSW. This increases the DRX and develops finer grains.

(4) The CA model can analyze the dislocation accumulation map, nucleation, and grain growth phase of DRX during FSW and FSVW, and also provide precisely the grain size and microstructure properties of the joint zone.

(5) The strain distribution increases and grain size reduces as vibration frequency improves during the FSVW. The CA model indicates that the DRX process enhances as the vibration frequency and strain rate increase.

References

[1] DADAEI M, OMIDVAR H, BAGHERI B, JAHAZI M, ABBASI M. The effect of SiC/Al_2O_3 particles used during FSP on mechanical properties of AZ91 magnesium alloy [J]. International Journal of Materials Research, 2014, 105: 369−374. https://doi.org/10.3139/146.111025.

[2] ZENG R, DIRTZEL W, ZETTLER R, GAN W, SUN X. Microstructure evolution and delayed hydride cracking of FSW-AZ31 magnesium alloy during SSRT [J]. Transactions of Nonferrous Metals Society of China, 2014, 24(10): 3060−3069. https://doi.org/10.1016/S1003-6326(14)63443-9.

[3] GARG A, RATUR M, BHATTACHARYA A. Metallurgical behavior and variation of vibro-acoustic signal during preheating assisted friction stir welding between AA6061-T6 and AA7075-T651 alloys [J]. Transactions of Nonferrous Metals Society of China, 2019, 29: 1610−1620. https://doi.org/10.1016/S1003-6326(19)65068-5.

[4] JAFARI M, ABBASI M, POURSINA D, GHEYSARIAN A, BAGHERI B. Microstructures and mechanical properties of friction stir welded dissimilar steel−copper joints [J]. Journal of Mechanical Science and Technology, 2017, 31(3): 1135−1142. https://doi.org/10.1007/s12206-016-1217-z.

[5] ANDRADE D G, LEITAO C, DIALAMI N, CHIUMENTI M, RODRIGUES D M. Modelling torque and temperature in friction stir welding of aluminium alloys [J]. International Journal of Mechanical Science, 2020, 182: 105725. https://doi.org/10.1016/j.ijmecsci.2020.105725.

[6] JAIN R, PAL S K, SINGH S B. Investigation on effect of pin shapes on temperature, material flow and forces during friction stir welding: A simulation study [J]. Proceedings of the Institution of Mechanical Engineering, Part B: Journal of Engineering Manufacture, 2019, 233: 1993−2006. https://doi.org/10.1177/0954405418805615.

[7] SHI L, WU C S, LIU H J. Modeling the material flow and heat transfer in reverse dualrotation friction stir welding [J]. Journal of Materials Engineering and Performance, 2014, 23: 2918−2929. https://doi.org/10.1007/s11665-014-1042-4.

[8] JAIN R, PAL S K, SINGH S B. Finite element simulation of pin shape influence on material flow, forces in friction stir welding [J]. International Journal of Advanced Manufacturing and Technology, 2018, 94: 1781−1797. https://doi.org/10.1007/s00170-017-0215-3.

[9] MARDALIZADEH M, KHANDAEI M, SAFARKHANIAN M A. Floating-bobbin-tool friction stir welding of 20-mm-thick AA5456-H112 plates: Microstructure and weld strength [J]. Journal of Materials Engineering and Performance, 2021, 30: 3284−3297. https://doi.org/10.1007/s11665-021- 05669-5.

[10] DIALAMI N, CERVERA M, CHIUMENTI M, de SARACIBAR C A, de SARACIBAR C. A fast and accurate two-stage strategy to evaluate the effect of the pin tool profile on metal flow, torque and forces in friction stir welding [J]. International Journal of Mechanical Science, 2017, 122: 215−227. https://doi.org/10.1016/j.ijmecsci.2016. 12.016.

[11] KEIVANI R, BAGHERI B, SHARIFI F, KETABCHI M, ABBASI M. Effects of pin angle and preheating on temperature distribution during friction stir welding operation [J]. Transactions of Nonferrous Metals Society of China, 2013, 23: 2708−2713. https://doi.org/10.1016/S1003-6326(13)62788-0.

[12] ABBASI M, BAGHERI B, KEIVANI R. Thermal analysis of friction stir welding process and investigation into affective parameters using simulation [J]. Journal of Mechanical Science and Technology, 2015, 29(2): 861−866. https://doi.org/10.1007/s12206-015-0149-3.

[13] MARZBAND J, AKBARI M, ASADI P, SAFAEE S. Characterization of the influence of tool pin profile on microstructural and mechanical properties of friction stir welding [J]. Metallurgical Materials Transaction B, 2015, 45(5): 1887−1894. https://doi.org/10.1007/s11663-014-0089-9.

[14] BAROONI O, ABBASI M, GIVI M, BAGHERI B. New method to improve the microstructure and mechanical properties of joint obtained using FSW [J]. International Journal of Advanced Manufacturing and Technology, 2017, 93: 4371−4378. https://doi.org/10.1007/s00170-017-0810-3.

[15] VALVI R S H, KRISHNAN A, DAS S, NARAYANA R G. Prediction of microstructural features and forming of friction stir welded sheets using cellular automata finite element (CAFE) approach [J]. International Journal of Materials

Forming, 2016, 9: 115−129. https://doi.org/10.1007/s12289-015-1216-0.

[16] LIU X, LI L X, HE F Y, ZHOU J, ZHU B W, ZHANG L Q. Simulation on dynamic recrystallization behavior of AZ31 magnesium alloy using cellular automaton method coupling Laasraoui−Jonas model [J]. Transactions of Nonferrous Metals Society of China, 2013, 23: 2692−2699. https://doi.org/10.1016/S1003-6326.

[17] PROSGOLITIS C G, LAMBRAOS S G, ZERVAKI A D. Phase-field modeling of nugget zone for a AZ31−Mg-alloy friction stir weld [J]. Journal of Materials Engineering and Performance, 2018, 27: 5102−5113. https://doi.org/10.1007/s11665-018-3471-y.

[18] AFSHARI E, SERAJZADEH S. Simulation of static recrystallization after cold side-pressing of low carbon steels using cellular automata [J]. Journal of Materials Engineering and Performance, 2012, 21(8): 1553−1561. https://doi.org/10.1007/s11665-011-0063-5.

[19] ASADI P, GIVI M K B, AKBARI M. Simulation of dynamic recrystallization process during friction stir welding of AZ91 magnesium alloy [J]. International Journal of Advanced Manufacturing and Technology, 2015, 83: 301−311. https://doi.org/10.1007/s00170-015-7595-z.

[20] HUNG J C, LIN C C. Investigations on the material property changes of ultrasonic-vibration assisted aluminum alloy upsetting [J]. Materials Design, 2013, 45: 412−420. https://doi.org/10.1016/j.matdes.2012.07.021.

[21] MENG B, CAO B N, WAN M, WANG C J, SHAN D B. Constitutive behavior and microstructural evolution in ultrasonic vibration assisted deformation of ultrathin super alloy sheet [J]. International Journal of Mechanical Science, 2019, 157−158: 609−618. https://doi.org/10.1016/j.ijmecsci.2019.05.009.

[22] KUMAR SAXENA S, WU C S, PADHYGK G K, DING W. Application of ultrasonic vibrations in welding and metal processing: A status review [J]. Journal of Manufacturing Processes, 2017, 26: 295−322. https://doi.org/10.1016/j.jmapro.2017.02.027.

[23] GAO S, WU C S, PADHY G K. Material flow, microstructure and mechanical properties of friction stir welded AA 2024-T3 enhanced by ultrasonic vibrations [J]. Journal of Manufacturing Processes, 2017, 30: 385−395. https://doi.org/10.1016/j.jmapro.2017.10.008.

[24] SHI L, WU C S, LIU X C. Modeling the effects of ultrasonic vibration on friction stir welding [J]. Journal of Materials Processing and Technology, 2015, 222: 91−102. https://doi.org/10.1016/j.jmatprotec.2015.03.002.

[25] LIU Z L, MENG X C, JI S D, LI Z W, WANG L. Improving tensile properties of Al/Mg joint by smashing intermetallic compounds via ultrasonic-assisted stationary shoulder friction stir welding [J]. Journal of Manufacturing and Processes, 2018, 31: 552−559. https://doi.org/10.1016/j.jmapro.2017.12.022.

[26] LIU X C, WU C S, PADHY G K. Improved weld macrosection, microstructure and mechanical properties of 2024Al-T4 butt joints in ultrasonic vibration enhanced friction stir welding [J]. Science Technology Welding and Joining, 2015, 20: 345−352. https://doi.org/10.1179/1362171815Y.0000000021.

[27] SHI L, WU C S, GAO S. Analysis of welding load reduction in ultrasonic vibration-enhanced friction stir welding [J]. International Journal of Advanced Manufacturing and Technology, 2018, 99: 373−385. https://doi.org/10.1007/s00170-018- 2472-1.

[28] YANG C L, WU C S, SHI L. Analysis of friction reduction effect due to ultrasonic vibration exerted in friction stir welding [J]. Journal of Manufacturing Processes, 2018, 35: 118−126. https://doi.org/10.1016/j.jmapro.2018.07.025.

[29] ZHAO W, WU C H, SHI L. Acoustic induced antifriction and its effect on thermo-mechanical behavior in ultrasonic assisted friction stir welding [J]. International Journal of Mechanical Sciences, 2021, 190: 106039. https://doi.org/10.1016/j.ijmecsci.2020.106039.

[30] ZHANG Z, ZHANG H W. A fully coupled thermo-mechanical model of friction stir welding [J]. International Journal of Advanced Manufacturing and Technology, 2008, 37: 279−293. https://doi.org/10.1007/s00170-007-0971-6.

[31] DAI Q S, DENG Y L, TANG J G, WANG Y. Deformation characteristics and strain-compensated constitutive equation for AA5083 aluminum alloy under hot compression [J]. Transactions of Nonferrous Metals Society of China, 2019, 29: 2252−2261. https://doi.org/10.1016/S1003-6326(19)65131-9.

[32] SALUJA R S, NARAYANAN RG, DAS S. Cellular automata finite element (CAFE) model to predict the forming of friction stir welded blanks [J]. Computational Materials Science, 2012, 58: 87−100. https://doi.org/10.1016/j.commatsci.2012.01.036.

[33] HALLBERG H. Approaches to modeling of recrystallization [J]. Metal, 2011, 1: 16−48. https://doi.org/10.3390/met1010016.

[34] CHEN F, CUI Z H, OU H, LONG H. Mesoscale modeling and simulation of microstructure evolution during dynamic recrystallization of a Ni-based superalloy [J]. Applied Physics A, 2016, 122: 890. https://doi.org/10.1007/s00339-016-0404-1.

[35] AKBARI M, ASADI P, GIVI M K B, ZOLGHADR P. A cellular automaton model for microstructural simulation of friction stir welded AZ91 magnesium alloy [J]. Modeling and Simulation Materials Science and Engineering, 2016, 24: 35012. https://doi.org/10.1088/0965-0393/24/3/035012.

[36] DING H, SHIN Y C. Dislocation density-based grain refinement modeling of orthogonal cutting of titanium [J]. ASME Journal of Manufacturing Science and Engineering, 2014, 136(4): 41003. https://doi.org/10.1115/1.4027207.

[37] DING R, GUO Z X. Coupled quantitative simulation of microstructural evolution and plastic flow during dynamic recrystallization [J]. Acta Meterialia, 2001, 49: 3163−3175. https://doi.org/10.1016/S1359-6454(01)00233-6.

[38] LV B J, PENG J, SHI D W, TANG A T, PAN F S. Constitutive modeling of dynamic recrystallization kinetics and processing maps of Mg−2.0Zn−0.3Zr alloy based on true stress−strain curves [J]. Materials Science Engineering A, 2013, 560: 727−733. https://doi.org/10.1016/j.msea.2012.10.025.

[39] XU Y, HU LX, SUN Y. Dynamic recrystallization kinetics of as-cast AZ91D alloy [J]. Transactions of Nonferrous Metals Society of China, 2014, 24: 1683−1689. https://doi.org/

10.1016/S1003-6326(14)63241-6.

[40] QIAN M, GUO Z X. Cellular automata simulation of microstructural evolution during dynamic recrystallization of an HY-100 steel [J]. Materials Science and Engineering A, 2004, 365: 180−185. https://doi.org/10.1016/j.msea.2003.09.025.

[41] XIAO M N, ZHENG C W, LI D Z, LI Y Y. A simulation of dynamic recrystallization by coupling a cellular automaton method with a topology deformation technique [J]. Computational Materials Science, 2008, 41(3): 366−374. https://doi.org/10.1016/j.commatsci.2007.04.021.

[42] SONG K J, FANG K, DONG Z B, ZHANG X H, WEI Y H. Cellular automaton modelling of dynamic recrystallisation microstructure evolution during friction stir welding of titanium alloy [J]. Materials Science and Technology, 2013, 700−711. https://doi.org/10.1179/1743284713Y.0000000389.

[43] ZHANG Y, JIANG S H, LIANG Y, LI H. Simulation of dynamic recrystallization of NiTi shape memory alloy during hot compression deformation based on cellular automaton [J]. Computational Materials Science, 2013, 71: 124−134. https://doi.org/10.1016/j.commatsci.2013.01.019.

[44] CHEN F, CUI Z H. Mesoscale simulation of microstructure evolution during multi-stage hot forging processes [J]. Modelling Simulation in Materials Science and Engineering, 2012, 20: 045006. https://doi.org/10.1088/0965-0393/20/4/045008.

[45] YAO Z, KIM G Y, WANG Z, FAIDLEY L, ZOU Q, MEI D, CHEN Z. Acoustic softening and residual hardening in aluminum: modeling and experiments [J]. International Journal of Plasticity, 2012, 39: 75−87. https://doi.org/10.1016/j.ijplas.2012.06.003.

[46] BAGHERI B, ABBASI M, ABDOLLAHZADEH A, KOKABI A H. Effect of vibration on machining and mechanical properties of AZ91 alloy during FSP: Modeling and experiments [J]. International Journal of Material Forming, 2020. https://doi.org/10.1007/s12289-020-01551-2.

[47] SHI L, WU S C, GAO S, PADHY G K. Modified constitutive equation for use in modeling the ultrasonic vibration enhanced friction stir welding process [J]. Scripta Materialia, 2016, 119: 21−26. https://doi.org/10.1016/j.scriptamat.2016.03.023.

[48] BAGHERI B, ABBASI M, HAMZELOO R. The investigation into vibration effect on microstructure and mechanical characteristics of friction stir spot vibration welded aluminum: Simulation and experiment [J]. Proceedings Institute Mechanical Engineering, Part C: Journal of Mechanical Engineering, 2020, 234(9): 1809−1822. https://doi.org/10.1177/0954406219900194.

[49] SAMANTA A, SHEN N G, JI H P, WANG W M, LI J J, DING H T. Cellular automation simulation of microstructure evolution for friction stir blind riveting [J]. Journal of Manufacturing Science and Engineering, 2018, 140: 031016. https://doi.org/ 10.1115/1.4038576.

[50] BAGHERI B, ABDOLLAHZADEH A, ABBASI M, KOKABI A H. Numerical analysis of vibration effect on friction stir welding by smoothed particle hydrodynamics (SPH) [J]. International Journal Advanced Manufacturing Technology, 2020, 110: 209−228. https://doi.org/10.1007/s00170-020-05839-0.

[51] MORISADA Y, IMAIZUMI T, FUJII H. Clarification of material flow and defect formation during friction stir welding [J]. Science and Technology of Welding and Joining, 2015, 20: 130−137. https://doi.org/10.1179/1362171814Y.0000000266.

[52] CHEN G Q, FENG Z L, ZHU Y C, SHI Q Y. An alternative frictional boundary condition for computational fluid dynamics simulation of friction stir welding [J]. Journal of Materials Engineering and Performance, 2016, 25: 4016−4023. https://doi.org/10.1007/s11665-016-2219-9.

[53] KUMAR R, PANCHOLI V, BHARTI R P. Material flow visualization and determination of strain rate during friction stir welding [J]. Journal of Materials Processing and Technology, 2018, 255: 470−476. https://doi.org/10.1016/j.jmatprotec.2017.12.034.

[54] YANG C H, WU C S, SHI L. Phase-field modelling of dynamic recrystallization process during friction stir welding of aluminium alloys [J]. Science and Technology of Welding and Joining, 2019, 345−358. https://doi.org/10.1080/13621718.2019.1706261.

[55] ABDOLLAHZADEH A, SHOKUFAR A, OMIDVAR H, CABRERA J M, SOLONIN A, OSTOVARI A, ABBASI M. Structural evaluation and mechanical properties of AZ31/SiC nano-composite produced by friction stir welding process, at various welding speeds [J]. Processing of the Institution of Mechanical Engineering, Part L: Journal of Materials Design and Application, 2019. http://dx.doi.org/10.1177/1464420717708485.

[56] WU Q, ZHANG Z. Precipitation-induced grain growth simulation of friction-stir-welded AA6082-T6 [J]. Journal of Materials Engineering and Performance, 2017, 26: 2179−2189. http://dx.doi. org/10.1007/s11665-017-2639-1.

[57] FOULADI S, ABBASI M. The effect of friction stir vibration welding process on characteristics of SiO_2 incorporated joint [J]. Journal of Materials Processing Technology, 2017, 243: 23−30. http://dx.doi.org/10.1016/j.jmatprotec.2016.12.005.

[58] BAGHERI B, ABBASI M, DADAEI M. Mechanical behavior and microstructure of AA6061-T6 joints made by friction stir vibration welding [J]. Journal of Materials Engineering and Performance, 2020, 29: 1165−1175. https://doi.org/10.1007/s11665-020-04639-7.

[59] ABDOLLAHZADEH A, BAGHERI B, ABBASI A, KOKABI A H, MOGHADDAM A O. Comparison of the weldability of AA6061-T6 joint under different friction stir welding conditions [J]. Journal of Material Engineering and Performance, 2020, 30: 1110−1127. https://doi.org/10.1007/s11665-020-05379-4.

[60] ABBASI M, GIVI M, BAGHERI B. Application of vibration to enhance efficiency of friction stir processing [J]. Transactions of Nonferrous Metals Society of China, 2019, 29: 1393−1400. https://doi.org/10.1016/S1003-6326(19)65046-6.

[61] BAGHERI B, ABBASI M, ABDOLLAHZADEH A, MIRSALEHI S E. The effect of second phase particle size and presence of vibration on AZ91/SiC surface composite layer produced by FSP [J]. Transactions of Nonferrous Metals Society of China, 2020, 30: 905−916. https://doi.org/10.1016/S1003-6326(20)65264-5.

[62] CHEN F, CUI Z S, LIU J, CHEN W, CHEN S J. Mesoscale simulation of the high temperature austenitizing and dynamic recrystallization by coupling a cellular automaton with a topology deformation technique [J]. Materials Science Engineering A, 2010, 527: 5539−5549. https://doi.org/10.1016/j.msea.2010.05.021.

[63] ABBASI M, ABDOLLAHZADEH A, BAGHERI B, MOGHADDAM A O, SHARIFI F, DADAEI M. Study on the effect of the welding environment on the dynamic recrystallization phenomenon and residual stresses during the FSW process of aluminum alloy [J]. Proceedings of the Institution of Mechanical Engineers, Part L: Journal of Materials Design and Applications, 2021, 238: 1809−1826. https://doi.org/10.1177/14644207211025113.

[64] HU Y, LIU H, FUJII H, USHIODA K. Effect of ultrasound on microstructure evolution of friction stir welded aluminum alloys [J]. Journal of Manufacturing Processes, 2020, 56: 362−371. https://doi.org/10.1016/j.jmapro.2020.05.005.

振动搅拌摩擦焊镁合金动态再结晶过程的模拟与实验研究

Mahmoud ABBASI[1], Behrouz BAGHERI[2], Farzaneh SHARIFI[3]

1. Faculty of Engineering, University of Kashan, Kashan, Iran;

2. Department of Mining and Metallurgy, Amirkabir University of Technology, Tehran, Iran;

3. School of Mechanical and Materials Engineering, Washington State University, Pullman, USA

摘　要：采用二维元胞自动机(CA)模型分析机械振动对 AZ91 合金在搅拌摩擦焊(FSW)过程中组织演变的影响。将模拟结果，即晶粒拓扑结构、粒度分布、平均晶粒度以及动态再结晶(DRX)分数与实测数据进行比较。结果显示，有限元分析结果与实验数据具有充分的相似性，CA 方法可用于搅拌摩擦焊 AZ91 合金组织演变的分析。与 FSW 相比，振动搅拌摩擦焊(FSVW) 处理的样品中位错密度更高，形核和晶粒长大也更快。对 FSVW 过程中不同振动频率下的晶粒度改变和 DRX 现象经过详细模拟后发现，振动使形核开始时间提前，随着振动频率的提高，孕育期和再结晶的比例降低。

关键词：搅拌摩擦焊；振动；模拟；晶粒度；动态再结晶；元胞自动机模型

(Edited by Bing YANG)